J. Fluid Mech. (2023), *vol*. 975, A17, doi:10.1017/jfm.2023.662

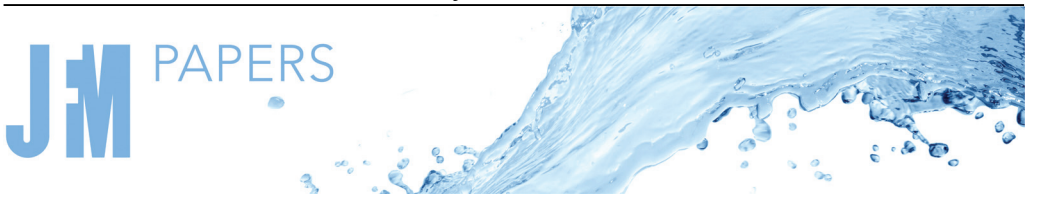

Energy flux and high-order statistics of hydrodynamic turbulence

Yuri V. Lvov[1],† **and Victor S. L'vov**[2]

[1]Department of Mathematical Sciences, Rensselaer Polytechnic Institute, Troy, NY 12180, USA

[2]Department of Chemical and Biological Physics, Weizmann Institute of Science, Rehovot 76100, Israel

(Received 10 March 2023; revised 28 July 2023; accepted 3 August 2023)

We use the Dyson–Wyld diagrammatic technique to analyse the infinite series for the correlation functions of the velocity in hydrodynamic turbulence. We demonstrate the fundamental role played by the triple correlator of the velocity in determining the entire statistics of the hydrodynamic turbulence. All higher-order correlation functions are expressed through the triple correlator. This is shown through the suggested triangular re-summation of the infinite diagrammatic series for multi-point correlation functions. The triangular re-summation is the next logical step after the Dyson–Wyld line re-summation for the Green's function and the double correlator. In particular, it allows us to explain why the inverse cascade of the two-dimensional hydrodynamic turbulence is close to Gaussian. Since the triple correlator dictates the flux of energy ε through the scales, we support the Kolmogorov-1941 idea that ε is one of the main characteristics of hydrodynamic turbulence.

Key words: turbulence theory, Navier–Stokes equations

1. Introduction

Investigation of the statistical properties of hydrodynamic turbulence has a long and exciting history (Frisch 1995). The developed hydrodynamic turbulence may be characterized by three fundamental quantities: (i) the double correlation of the velocity (in the wave vector, frequency representation $\boldsymbol{q} \equiv \{\boldsymbol{k}, \omega\}$) ${}^2\mathcal{F}(\boldsymbol{q})$, characterizing the energy distribution of k-eddies of scale $\ell \simeq 1/k$; (ii) the characteristic time scale $\tau(\boldsymbol{k})$ of the response of the k-eddies to the external perturbation, given by the Green's function $\mathcal{G}(\boldsymbol{q})$; (iii) the triple correlation ${}^3\mathcal{F}(\boldsymbol{q}_1, \boldsymbol{q}_2, \boldsymbol{q}_3)$, responsible for the energy flux across the scale $\ell \simeq k_1^{-1} \simeq k_2^{-1} \simeq k_3^{-1}$.

† Email address for correspondence: lvovy@rpi.edu

A systematic way to analyse these objects was suggested by Wyld (1961), who developed a diagrammatic method to treat infinite perturbation series for the response (Green's) and correlation functions of the velocity field. The essence of a diagrammatic technique is in a graphical representation (diagrams) of infinite perturbation series. The key advantage of the diagrammatic technique is that it is possible to draw and analyse diagrams for the higher-order correlation function without deriving explicitly the corresponding analytical expressions first.

Basic objects in the Wyld technique are the so-called 'bare' Green's function $\mathcal{G}_0(\boldsymbol{q})$ and 'bare' second-order correlation function ${}^2\mathcal{F}_0(\boldsymbol{q})$. These bare objects depend on the kinematic viscosity ν. A crucial step forward was the Dyson–Wyld line re-summation, which allows one to replace in all remaining diagrams the bare kinematic viscosity ν by what is called 'dressed by interaction turbulent viscosity' ν_{turb} that accounts for the main mechanism of the eddy damping due to the energy exchange between scales. From a physical viewpoint, this means that besides accounting for small damping of energy of eddies of a given scale due to kinematic viscosity, we account for a much stronger effect of their interaction with all the rest of the turbulent eddies, in the mean field approximation, known in the physics of turbulence as an approximation of turbulent viscosity. Mathematically, this is equivalent to replacing the initial expansion parameter $Re \gg 1$, where $Re \propto (1/\nu)$ is the Reynolds number, by the parameter $Re_{turb} \propto 1/\nu_{turb} = O(1)$. As a result, the re-summed diagrams involve only dressed objects: Green's function $\mathcal{G}(\boldsymbol{q})$, and simultaneous correlators ${}^2\mathcal{F}(\boldsymbol{q})$ instead of their bare counterparts $\mathcal{G}_0(\boldsymbol{q})$, ${}^2F_0(\boldsymbol{k})$ involving only $\nu \ll \nu_{turb}$. This kind of procedure in diagrammatic techniques is called dressing. It is well known that the dressing rearranges the terms in the perturbation expansion by moving the higher-order terms to lower orders and arranging them in the 'dressed' objects. Therefore, the infinite diagrammatic series becomes better ordered, more physically transparent, and presumably less divergent. Nevertheless, the series for ${}^3\mathcal{F}(\boldsymbol{q}_1, \boldsymbol{q}_2, \boldsymbol{q}_3)$, remains 'undressed' in the sense that it can be expressed in terms of the 'bare' ${}^3\mathcal{F}_0(\boldsymbol{q}_1, \boldsymbol{q}_2, \boldsymbol{q}_3)$, proportional to the original ('bare') interaction amplitude $\boldsymbol{V}(\boldsymbol{k}_1, \boldsymbol{k}_2, \boldsymbol{k}_3)$ in the Navier–Stokes equations (Frisch 1995; Pope 2000).

Analyses of the topological properties of the resulting diagrams allowed us to suggest in this paper a natural next logical step after the Dyson–Wyld line re-summation, namely the triangular re-summation. To find the triangular re-summation would be impossible, or near impossible, by studying analytical formulas for the perturbation expansion. The triangular re-summation expresses the simultaneous triple correlator ${}^3F(\boldsymbol{k}_1, \boldsymbol{k}_2, \boldsymbol{k}_3)$ in terms of three dressed objects, $\mathcal{G}(\boldsymbol{q})$ and simultaneous correlators ${}^2F(\boldsymbol{k})$ and ${}^3F(\boldsymbol{k}_1, \boldsymbol{k}_2, \boldsymbol{k}_3)$ itself. Since this dressing is the result of combining higher-order terms into these three dressed objects, the resulting infinite diagrammatic series is less likely to diverge. Moreover, we show that the quadruple and higher-order correlators ${}^4F$, ${}^5F$, etc. are also proportional to the powers of ${}^3F$. Consequently, the fourth quadruple and higher-order correlators do vanish if ${}^3F = 0$. In the thermodynamic equilibrium, ${}^3F = 0$, so in the equilibrium, all cumulants are zero and statistics of turbulence become Gaussian order by order. To reach these goals, we revisit carefully the Wyld diagrammatic approach from the very beginning, paying special attention to the numerical prefactors of the diagrams, which are crucially important for their further re-summations.

The principal advantage of the proposed triangular re-summation is that it expresses all simultaneous correlation functions through the dressed simultaneous triple correlator. The triple correlator determines the flux of energy over scales. Therefore, all simultaneous

correlators depend on the energy flux. This conclusion illustrates the unique importance of the energy fluxes through the spectral space, and can be considered as a generalization of Kolmogorov-1941 dimensional reasoning (Kolmogorov 1941; Frisch 1995) that related the energy distribution over scales (i.e. the second-order velocity correlator) with the energy flux.

Having developed the theory for multi-point correlators, we consider in more detail the two-dimensional (2-D) turbulence, which allows the presentation of the Navier–Stokes equation in a scalar form (Kraichnan & Montgomery 1980). Remarkably, the 2-D turbulence serves as an idealized model for many natural flow phenomena, including geophysical flows in the atmosphere, oceans and magnetosphere. Set-ups that are quite close to 2-D turbulence were realized experimentally (Tabeling 2002). It is observed in both direct numerical simulations and experiments that the statistics of 2-D turbulence is surprisingly close to the Gaussian (Boffeta, Celani & Vergassola 2000; Boffetta & Ecke 2012). The natural explanation of this fact follows from our results. First, we show that ${}^{3}F$ vanishes in the thermodynamic equilibrium. Second, all cumulants ${}^{n}F$ are proportional to powers of ${}^{3}F$ and thus also vanish in the equilibrium, as expected in the Gaussian statistics that takes place in the equilibrium (see e.g. Landau & Lifshitz 1980). This exposes the explicit mechanism of how Gaussian statistics of turbulence in equilibrium is order-by-order consistent with the diagrammatic expansion. Finally, because in fractional dimension $d = 4/3$ the scaling index of the inverse energy cascade ${}^{2}F(k) \propto k^2$ coincides with that in the thermodynamic equilibrium (with the enstrophy equipartition between scales) we demonstrate Gaussianity of the inverse energy cascade in $d = 4/3$. We show also that the triple correlator ${}^{3}F \propto (d - 4/3)$ and thus all cumulants ${}^{n}F$ are small near $d = 4/3$, being proportional to the powers of $(d - 4/3)$. This explains the closeness of the inverse cascade of the 2-D turbulence close to the Gaussianity also in the physical case $d = 2$, as noticed in L'vov, Pomyalov & Procaccia (2002).

The paper is organized as follows. In § 2.1, we set the stage by introducing a scalar equation for the 2-D and three-dimensional (3-D) turbulence. In § 2.2, we discuss the perturbation expansion for the field amplitudes, showing that the prefactors in resulting tree diagrams are equal to $1/N$, where N is the number of elements in the symmetry group of each particular tree diagram. Many diagrams do not have any symmetries apart from the identity transformation, so $N = 1$. If the diagram is symmetric with respect to a certain line, then there will be two symmetry elements, reflection and identity, so that $N = 2$ and so on. This factor will be considered in detail in the body of the paper. We refer to this fact as the '$1/N$ symmetry' rule. We show that the $1/N$ symmetry rule is valid for all types of diagrams and for any of their fragments.

The next step, presented in § 2.3, is the procedure of 'gluing' of the n tree diagram that results in diagrams for the n-point, different-time correlation functions ${}^{n}\mathcal{F}$ for which the symmetry rule for the prefactors is also applicable.

Analysis of the resulting diagrams leads to formulations in § 2.4 of diagrammatic rules for ${}^{n}\mathcal{F}$ that allow one to find them in arbitrary order without sequential analysis of all previous orders in the expansion. In principle, this allows one to skip reading §§ 2.2, 2.3 and 2.4, and to look only at the final diagrams for the correlation functions.

In § 3, we reduce the resulting diagrams for the different-time correlations ${}^{n}\mathcal{F}$ (in the $\boldsymbol{q} \equiv (\boldsymbol{k}, \omega)$ representation) to the single-time domain, denoted as ${}^{n}F$. For this goal, we used the relation ${}^{2}\mathcal{F}(\boldsymbol{k}, \omega) \propto \mathrm{Re}\{\mathcal{G}(\boldsymbol{k}, \omega)\}$, where Re denotes the real part of a complex quantity. This expression follows from Wyld re-summation. The resulting 'extended' set

of diagrams for simultaneous correlators ${}^nF$ involves simultaneous ${}^2F(\boldsymbol{k})$ and the Green's functions $\mathcal{G}(\boldsymbol{k},\omega)$. Once again, the prefactors are given by the $1/N$ symmetry rule.

The numerical value of the prefactors in the extended set of diagrams for ${}^nF$, given by the $1/N$ symmetry rule, allows us to group them into groups of three (triads) such that each group appears as a diagram for ${}^3F$. Interestingly, some diagrams participate in more than one triad. Consequently, grouping diagrams into triads to form a triple correlator is a non-trivial task. Finally, we discovered how to find a set of triads that can be summed up to the full series for ${}^3F$.

Note that the topological structure of the diagrammatic series is defined by the quadratic nonlinearity of the Navier–Stokes equation with the interaction vertex satisfying the Jacobi identity. The Jacobi identity is a mathematical manifestation of energy conservation in hydrodynamic turbulence. The 2-D turbulence has an additional Jacobi identity manifesting the enstrophy conservation. Therefore, our conclusions are applicable to both 3-D and 2-D turbulence.

2. Diagrammatic technique for strongly interacting fields

2.1. *Basic equation of motion for 3-D and 2-D hydrodynamics*

This paper is based on the Wyld diagrammatic technique for hydrodynamic turbulence (Wyld 1961) generalized by Martin, Siggia & Rose (1973) and by Zakharov & L'vov (1975). Its detailed review is available in L'vov & Procaccia (1995). Generally speaking, the proposed technique can be applied straightforwardly to any integer dimensions, including either 2-D or 3-D turbulence that differs in the analytical form of the Navier–Stokes equations, as well as to other problems, for example, passive scalar. Its application for non-integer dimensions is more tricky and requires understanding how to perform integrations in non-integer dimensions; see e.g. L'vov *et al.* (2002).

In the 3-D case, the Euler equations for the velocity $\boldsymbol{v}(\boldsymbol{r},t)$ of an incompressible fluid with density $\rho=1$ have the well-known form (Landau & Lifshitz 2013)

$$\frac{\partial \boldsymbol{v}(\boldsymbol{r},t)}{\partial t}+(\boldsymbol{v}\cdot\boldsymbol{\nabla})\boldsymbol{v}+\boldsymbol{\nabla}p=0,\quad \boldsymbol{\nabla}\cdot\boldsymbol{v}=0. \tag{2.1a}$$

In the $(\boldsymbol{k},t)$ representation for the vector components $u^\alpha(\boldsymbol{k},t)$, (2.1*a*) can be rewritten as

$$\frac{\partial v^\alpha(\boldsymbol{k},t)}{\partial t}=\frac{1}{2}\int\frac{\mathrm{d}^3k_1\,\mathrm{d}^3k_2}{(2\pi)^2}\,\delta(\boldsymbol{\kappa}+\boldsymbol{\kappa}_1+\boldsymbol{\kappa}_2)\,\Gamma^{\alpha\beta\gamma}_{k12}\,u^{*\beta}_{\kappa_1}\,u^{*\gamma}_{\kappa_2}; \tag{2.1b}$$

see e.g. L'vov & Procaccia (1995). Here, $\Gamma^{\alpha\beta\gamma}_{k12}$ is the interaction amplitude

$$\Gamma^{\alpha\beta\gamma}_{k12}=\mathrm{i}\sum_{\alpha'}\left(\delta_{\alpha\alpha'}-\frac{k^\alpha k^{\alpha'}}{k^2}\right)(k^\beta\delta_{\alpha'\gamma}+k^\gamma\delta_{\alpha'\beta}), \tag{2.1c}$$

where $\delta_{\alpha\beta}$ is 1 if $\alpha=\beta$, and vanishes otherwise. Euler equation (2.1*a*) preserves the total energy of the flow

$$\mathcal{E}=\int|\boldsymbol{v}(\boldsymbol{r},t)|^2\,\mathrm{d}^3r=\int|\boldsymbol{u}(\boldsymbol{k},t)|^2\,\frac{\mathrm{d}^3k}{(2\pi)^3}. \tag{2.1d}$$

Therefore $\Gamma^{\alpha\beta\gamma}_{k12}$ satisfies Jacobi identity

$$\Gamma^{\alpha\beta\gamma}_{k12}+\Gamma^{\gamma\alpha\beta}_{2k1}+\Gamma^{\beta\gamma\alpha}_{12k}=0 \tag{2.1e}$$

on the surface $\boldsymbol{k}+\boldsymbol{k}_1+\boldsymbol{k}_2=0$.

The basic equations of motion for 2-D turbulence have a structure similar to the 3-D case (2.1). The 2-D turbulence may be represented as a scalar equation for the vorticity, which simplifies analytical expressions. Therefore, for the transparency of the presentation, we illustrate our formalism for the 2-D turbulence. In the present work, following L'vov *et al.* (2002), we consider the Euler equation for the vorticity equation in 2-D:

$$\partial\omega/\partial t + (\boldsymbol{u}\cdot\boldsymbol{\nabla})\omega = 0. \tag{2.2}$$

The velocity and vorticity of a 2-D flow may be derived from the stream function $\psi(\boldsymbol{x}, t)$ as $\boldsymbol{u}(\boldsymbol{x}, t) = -\boldsymbol{\nabla}\times\hat{\boldsymbol{z}}\,\psi(\hat{\boldsymbol{x}}, t)$ and $\omega(\boldsymbol{x}, t) = -\nabla^2\psi(\boldsymbol{x}, t)$, where $\hat{\boldsymbol{z}}$ is a unit vector orthogonal to the $\hat{\boldsymbol{x}}$-plane, and ∇^2 is the Laplacian operator in the plane. In the $\boldsymbol{k}$ representation, $a(\boldsymbol{k}, t) \equiv k\int \mathrm{d}\boldsymbol{R}\exp[-\mathrm{i}(\boldsymbol{R}\cdot\kappa)]\,\psi(\boldsymbol{R}, t)$. The Fourier transforms of $\boldsymbol{u}(\hat{\boldsymbol{x}}, t)$ and $\boldsymbol{\omega}(\hat{\boldsymbol{x}}, t)$ are denoted as $\boldsymbol{v}(\kappa, t)$ and $\Omega(\kappa, t)$, respectively. These Fourier transforms are expressed in terms $a(\kappa, t)$, re-designated for the shortness as $a_{\boldsymbol{k}}$: $\boldsymbol{v}(\kappa, t) = \mathrm{i}(\hat{\boldsymbol{z}}\times\hat{\kappa})a_\kappa$ and $\Omega(\kappa, t) = -ka_\kappa$, where $\hat{\kappa} = \kappa/k$. Now, by (2.2),

$$\left.\begin{aligned}
\frac{\partial a_\kappa}{\partial t} &= \int \frac{\mathrm{d}^2k_1\,\mathrm{d}^2k_2}{2\times 2\pi}\,\delta(\boldsymbol{\kappa}+\boldsymbol{\kappa}_1+\boldsymbol{\kappa}_2)\,V_{k12}a^*_{\kappa_1}a^*_{\kappa_2},\\
V_{k12} &= \frac{S_{k12}(k_2^2-k_1^2)}{2kk_1k_2}, \quad S_{k12}\equiv 2k_1k_2\sin\varphi_{12},\\
S_{k12} &= S_{2k1} = S_{12k} = -S_{k21} = -S_{1k2} = -S_{21k},\\
|S_{k12}| &= \sqrt{2(k^2k_1^2+k_1^2k_2^2+k_2^2k^2)-k^4-k_1^4-k_2^4}.
\end{aligned}\right\} \tag{2.3}$$

Here, the interaction amplitude (or 'vertex') V_{k12} is expressed via S_{k12}, where $|S_{k12}|/4$ is the area of the triangle formed by the vectors $\boldsymbol{\kappa}$, $\boldsymbol{\kappa}_1$ and $\boldsymbol{\kappa}_2$. Also, $\varphi_{12} = \varphi_1 - \varphi_2$, with φ_k, φ_1 and φ_2 the angles in the triangular plane between the x_1-axis and the vectors κ, κ_1 and κ_2, respectively. The vertex V_{k12} satisfies two Jacobi identities:

$$(V_{k12}+V_{2k1}+V_{12k}) = 0, \quad (k^2V_{k12}+k_2^2V_{2k1}+k_1^2V_{12k}) = 0. \tag{2.4a,b}$$

These two identities ensure the conservation of energy $\mathcal{E}$ in the inviscid forceless limit and the enstrophy $\mathcal{H}$ given by

$$\mathcal{E} \equiv \int |a_k|^2\,\frac{\mathrm{d}^2k}{(2\pi)^2}, \quad \mathcal{H} \equiv \int k^2|a_k|^2\,\frac{\mathrm{d}^2k}{(2\pi)^2}. \tag{2.5a,b}$$

Equation (2.3) describes the 2-D hydrodynamic turbulence. One sees that it has the same form as the 3-D (2.1), but without additional vector indices. Therefore, the results of this paper are applicable for both 2-D and 3-D turbulence. The concrete conclusions of our paper depend on the presence of the Jacobi identity for the symmetry of the matrix element. The 2-D turbulence has two quadratic integrals of motion (energy and enstrophy) and two Jacobi identities (2.4*a*,*b*) that reflect this fact. The 3-D turbulence has one integral of motion and just one Jacobi identity (2.1*e*). As shown e.g. by Kraichnan & Montgomery (1980), the physical properties of these two systems are different, yet they are described by the same technique and same triangular re-summation. To simplify our presentation, we focus in the paper on the 2-D turbulence.

Following Wyld (1961), we divide the world into the system under consideration and the thermostat. The action of the thermostat on the system is modelled by random noise $f(\boldsymbol{k}, t)$

and damping $\gamma_0(k)$. Then we replace $\partial a_\kappa/\partial t$ of (2.3) with $[\partial/\partial t + \gamma_0(\boldsymbol{k})]a_\kappa - f(\boldsymbol{k}, t)$, so that we obtain instead

$$\left[\frac{\partial}{\partial t} + \gamma_0(\boldsymbol{k})\right] a_\kappa = \int \frac{\mathrm{d}^2k_1\,\mathrm{d}^2k_2}{2\times 2\pi}\,\delta(\boldsymbol{\kappa}+\boldsymbol{\kappa}_1+\boldsymbol{\kappa}_2)\,V_{k12}a^*_{\kappa_1}a^*_{\kappa_2} + f(\boldsymbol{k}, t), \tag{2.6}$$

where the average statistics of the noise $f(\boldsymbol{k}, t)$ is assumed to satisfy $\langle f(\boldsymbol{k}, t)f(\boldsymbol{k}', t')\rangle \propto T\,\gamma_0(\boldsymbol{k}, t)\,\delta(\boldsymbol{k}-\boldsymbol{k}')\,\delta(t-t')$. Here, $\langle\cdot\rangle$ denotes an average with respect to the thermodynamic equilibrium ensemble with temperature T. The presence of the thermostat force and the damping allows (2.6) to have non-trivial solutions. After the Dyson–Wyld line-re-summation, described below, we will disconnect our system from the thermostat by taking the limit $\gamma_0(\boldsymbol{k}) \to 0$. It was shown by Wyld (1961) and Zakharov, L'vov & Starobinets (1975) that the result is independent of the thermostat parameters.

After the Fourier transformation with respect to time t, (2.6) in the $\boldsymbol{q} = (\boldsymbol{k}, \omega)$ representation becomes

$$a_{\boldsymbol{q}} = {}^0\mathcal{G}_{\boldsymbol{q}}\left[\frac{1}{2}\int \frac{\mathrm{d}\boldsymbol{q}_1\,\mathrm{d}\boldsymbol{q}_2}{(2\pi)^{d+1}}\,\delta^{d+1}_{q12}V_{k12}a^*_1a^*_2 + f_{\boldsymbol{q}}\right], \quad {}^0\mathcal{G}_{\boldsymbol{q}} = \mathrm{i}/[\omega + \mathrm{i}\,\gamma_0(\boldsymbol{k})]. \tag{2.7}$$

Here, ${}^0\mathcal{G}_{\boldsymbol{q}}$ is the bare Green's function, $\mathrm{d}\boldsymbol{q}_j \equiv \mathrm{d}^2k_j\,\mathrm{d}\omega_j$, and $V_{\boldsymbol{k12}} \equiv V(\boldsymbol{k}, \boldsymbol{k}_1, \boldsymbol{k}_2)$ is the interaction matrix element describing the strength of interactions between wavenumbers $\boldsymbol{k}$, $\boldsymbol{k}_1$ and $\boldsymbol{k}_2$.

2.2. *Iterative expansion for field variables $a_{\boldsymbol{q}}$*

Introducing the zero-order solution of this equation, ${}^0a_{\boldsymbol{q}} \equiv {}^0\mathcal{G}_{\boldsymbol{q}}f_{\boldsymbol{q}}$, we can get its iterative solution as a formal infinite series with respect to powers of ${}^0a_{\boldsymbol{q}}$: $a_{\boldsymbol{q}} = {}^0a_{\boldsymbol{q}} + {}^1a_{\boldsymbol{q}} + {}^2a_{\boldsymbol{q}} + {}^{3a}a_{\boldsymbol{q}} + {}^{3b}a_{\boldsymbol{q}} + {}^{4a}a_{\boldsymbol{q}} + {}^{4b}a_{\boldsymbol{q}} + {}^{4c}a_{\boldsymbol{q}} + \cdots$, where

$${}^1a_{\boldsymbol{q}} = \frac{{}^0\mathcal{G}_{\boldsymbol{q}}}{2}\int \frac{\mathrm{d}\boldsymbol{q}_1\,\mathrm{d}\boldsymbol{q}_2}{(2\pi)^{d+1}}\,\delta^{d+1}_{q56}V_{k56}a_5a_6 \;\Rightarrow\; {}^1a_{\boldsymbol{q}} \propto \frac{\mathcal{G}V}{2}\,a_5a_6, \tag{2.8a}$$

$${}^2a_{\boldsymbol{q}} = \frac{{}^0\mathcal{G}_{\boldsymbol{q}}}{2}\int \frac{\mathrm{d}\boldsymbol{q}_1\,\mathrm{d}\boldsymbol{q}_9}{(2\pi)^{d+1}}\,\delta^{d+1}_{q19}V_{k19}G_{\bar{1}}\int \frac{\mathrm{d}\boldsymbol{q}_2\,\mathrm{d}\boldsymbol{q}_3}{(2\pi)^{d+1}}\,\delta^{d+1}_{156}V_{156}a_9a_5a_6 \;\Rightarrow\; {}^2a_{\boldsymbol{q}} \propto \frac{(\mathcal{G}V)^2}{2}\,a_9a_5a_6, \tag{2.8b}$$

$${}^{3a}a_{\boldsymbol{q}} = {}^0\mathcal{G}_{\boldsymbol{q}}\int \frac{\mathrm{d}\boldsymbol{q}_1\,\mathrm{d}\boldsymbol{q}_5}{(2\pi)^{d+1}}\,\delta^{d+1}_{q15}V_{k15}\,{}^2a_1a_5 \;\Rightarrow\; {}^{3a}a_{\boldsymbol{q}} \propto \frac{(\mathcal{G}V)^3}{2}\,a_5a_6a_7a_8, \tag{2.8c}$$

$${}^{3b}a_{\boldsymbol{q}} = \frac{{}^0\mathcal{G}_{\boldsymbol{q}}}{2}\int \frac{\mathrm{d}\boldsymbol{q}_1\,\mathrm{d}\boldsymbol{q}_2}{(2\pi)^{d+1}}\,\delta^{d+1}_{q12}V_{k12}\,{}^1a_1\,{}^1a_2 \;\Rightarrow\; {}^{3b}a_{\boldsymbol{q}} \propto \frac{(GV)^3}{2^3}\,a_5a_6a_7a_8, \tag{2.8d}$$

$${}^{4a}a_{\boldsymbol{q}} = {}^0\mathcal{G}_{\boldsymbol{q}}\int \frac{\mathrm{d}\boldsymbol{q}_1\mathrm{d}\boldsymbol{q}_2}{(2\pi)^{d+1}}\,\delta^{d+1}_{q12}V_{k12}\,{}^{3a}a_1a_2 \;\Rightarrow\; {}^{4a}a_{\boldsymbol{q}} \propto \frac{(\mathcal{G}V)^3}{2}\,a_5a_6a_7a_8a_9, \tag{2.8e}$$

$${}^{4b}a_{\boldsymbol{q}} = {}^0\mathcal{G}_{\boldsymbol{q}}\int \frac{\mathrm{d}\boldsymbol{q}_1\,\mathrm{d}\boldsymbol{q}_2}{(2\pi)^{d+1}}\,\delta^{d+1}_{q12}V_{k12}\,{}^2a_1\,{}^1a_2 \Rightarrow\; {}^{4b}a_{\boldsymbol{q}} \propto \frac{(\mathcal{G}V)^3}{4}\,a_5a_6a_7a_8a_9, \tag{2.8f}$$

$${}^{4c}a_{\boldsymbol{q}} = {}^0\mathcal{G}_{\boldsymbol{q}}\int \frac{\mathrm{d}\boldsymbol{q}_1\,\mathrm{d}\boldsymbol{q}_2}{(2\pi)^{d+1}}\,\delta^{d+1}_{q12}V_{k12}\,{}^{3b}a_1a_2 \;\Rightarrow\; {}^{4c}a_{\boldsymbol{q}} \propto \frac{(\mathcal{G}V)^3}{8}\,a_5a_6a_7a_8a_9. \tag{2.8g}$$

Here, $\boldsymbol{q}_1 + \boldsymbol{q}_2 + \boldsymbol{q}_3 = 0$, $\mathcal{G}_j \equiv \mathcal{G}(\boldsymbol{q}_j)$ and $\mathcal{F}_j \equiv \mathcal{F}(\boldsymbol{q}_j)$, and a subscript with an overline denotes the negative of the corresponding wave vector, e.g. $\bar{j} = -\boldsymbol{q}_j$. Here, ${}^0a_{\boldsymbol{q}}$, ${}^1a_{\boldsymbol{q}}$, ${}^2a_{\boldsymbol{q}}$, ${}^3a_{\boldsymbol{q}}$

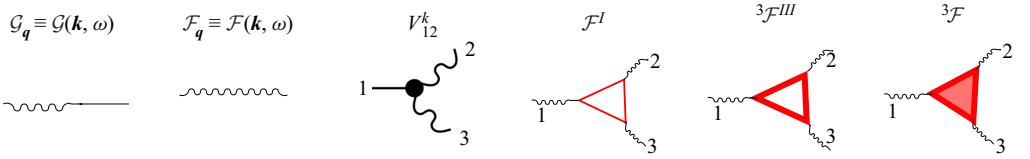

Figure 1. Graphical notation for the line re-summed Wyld's diagrammatic expansion. A short wavy line stands for the canonical variable $a_{\boldsymbol{q}} = a(\boldsymbol{k}, \omega)$. A straight line stands for the random force field $f(\boldsymbol{r}, t)$ that appears in (2.6). The Green's function $\mathcal{G}(\boldsymbol{k}, \omega)$, which is the response in the vorticity to some force, is made up of a short wavy line and a short straight line. A long wavy line represents double correlation functions $\mathcal{F}(\boldsymbol{k}, \omega)$ of the velocities. The vertex V_{123} (see (2.6)) is a fat dot with three tails. One straight tail belongs to the Green's function, and two wavy tails represent velocities. A triangle with three wavy lines represents simultaneous three-point correlators of the first order ${}^3\mathcal{F}^I_{123}$ (thin triangle) and of the third order ${}^3\mathcal{F}^{III}_{123}$ (thick triangle), and a fully dressed three-point correlator (in all orders) ${}^3\mathcal{F}_{123}$ (red filled triangle).

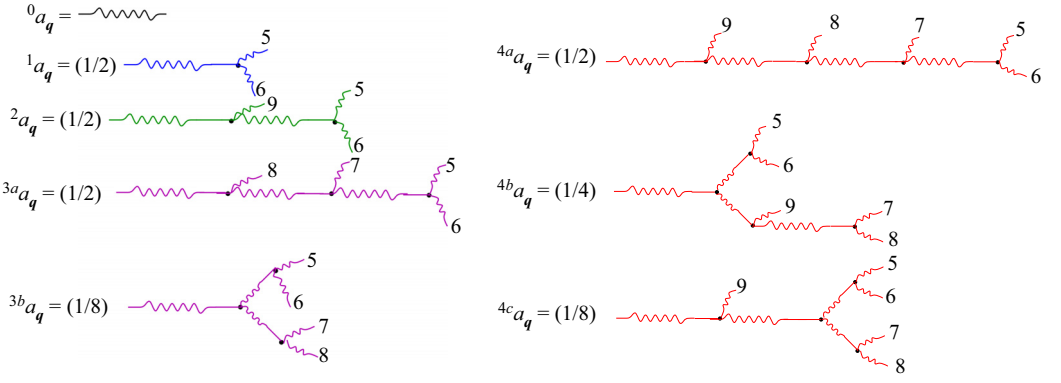

Figure 2. Graphical representation of the iterative expansion of $a_{\boldsymbol{q}}$, given by (2.8). We have reserved indices 1, 2, 3 and 4 ($\boldsymbol{q}_1$, $\boldsymbol{q}_2$, $\boldsymbol{q}_3$ and $\boldsymbol{q}_4$) for the arguments of the correlation functions. Therefore, we supplied wavy tails of the trees for ${}^n a_j$ with indices $j = 5, 6, \ldots$. Here, the left superscript ^{n} denotes the iteration order (the number of the vertices in trees).

and ${}^4a_{\boldsymbol{q}}$ are the zeroth-, first-, second-, third- and fourth-order iterations in the powers of interaction matrix element V; the number to the left of a denotes the order of the iteration. For the third and fourth orders, there are contributions of different topologies, so the letters 'a', 'b' and 'c' are used to differentiate between them.

Using graphical notation shown in figure 1, we can present each term in this series in a graphical form as a 'tree' diagram, as shown in figure 2. In these diagrams, the Green's function ${}^0G_{\boldsymbol{q}}$ is shown as a thin wavy–straight line, the ${}^0a_{\boldsymbol{q}}$ is shown as a short thin wavy line. The ${}^0a_{\boldsymbol{q}}$ are shown as thin wavy lines that are connected by vertex V_{123} shown as a fat dot '•'. The vertex has one straight tail, belonging to ${}^0G_{\boldsymbol{q}_1}$ and two wavy tails, belonging to ${}^0a_{\boldsymbol{q}_2}$ and ${}^0a_{\boldsymbol{q}_3}$. The key realization that gives birth to the diagrammatic technique is that instead of deriving (2.8), we could have had drawn all possible topologically different trees, without deriving (2.8) analytically first.

Analysing (2.8) and figure 2 with the trees, we see that the trees with the symmetrical elements have a numerical prefactor that is given by $1/N$, where N is the number of elements of the symmetry group of a diagram. This is a constructive demonstration of the $1/N$ symmetry rule for the trees. We will see this rule again when we consider diagrams for

the correlation function. The symmetry factor appears as a consequence of the $\boldsymbol{k}_1 \leftrightarrow \boldsymbol{k}_2$ symmetry and factor $1/2$ in the equation of motion (2.6). The rigorous proof of the $1/N$ symmetry rule is beyond the scope of the present paper. The $1/N$ symmetry rule will play a crucial role below, as it will lead to the natural grouping of the diagrams into triads. It would be much harder to see this rule by looking at analytical expressions alone.

The next important advantage of a diagrammatic technique is that from topological properties of the diagrams, one can make conclusions about the corresponding analytical expression without detailed analysis, and even perform a partial re-summation of diagrams with particular topological properties. This observation leads to the Dyson–Wyld line re-summation of reducible diagrams. A reducible diagram is one that contain fragments that can be disconnected from the rest of the diagram by cutting two lines. If these cut lines are wavy and straight ones, then the infinite sum of the corresponding fragments becomes 'dressed', Green's function $\mathcal{G}_{\boldsymbol{q}}$, defined as $\langle \partial a_{\boldsymbol{q}}/\partial f_{\boldsymbol{q}'} \rangle = (2\pi)^{d+1}\delta^{d+1}(\boldsymbol{q}-\boldsymbol{q}')\,\mathcal{G}_{\boldsymbol{q}}$. This Green's function can be presented as (see e.g. Wyld 1961; Zakharov, L'vov & Musher 1972; Martin *et al.* 1973)

$$\mathcal{G}_{\boldsymbol{q}} = \mathrm{i}/[\omega + \mathrm{i}\,\gamma_0(\boldsymbol{k}) - \Sigma_{\boldsymbol{q}}], \quad -\mathrm{Im}[\Sigma_{\boldsymbol{q}}] = \Gamma_{\boldsymbol{q}} = k^2\,\nu_{turb}(k), \tag{2.9a,b}$$

where the 'mass operator' $\Sigma_{\boldsymbol{q}}$ is an infinite sum of diagrams that begin and end with a vertex, and determines the 'turbulent' dissipation ν_{turb}. In the case where cut lines in the reducible diagram are two wavy lines, the infinite sum corresponds to the 'dressed' double correlator $\mathcal{F}_{\boldsymbol{q}}$, defined in the next subsection by (2.10*a*), shown in diagrams as long thick wavy lines.

After performing the Dyson–Wyld line re-summation, in the expansion (2.8) it is possible to replace the bare Green's functions ${}^{0}\mathcal{G}_{\boldsymbol{q}}$ by their dressed counterparts $\mathcal{G}_{\boldsymbol{q}}$. Furthermore, it is possible to replace the bare field ${}^{0}a_{\boldsymbol{q}}$ by the dressed field $a_{\boldsymbol{q}}$. Such modification presents the essence of 'dressing', i.e. moving terms from higher orders of the perturbation theory to lower orders, and combining them into the 'dressed' objects. The 'dressed' version of (2.8) will be used in the rest of the paper.

2.3. *Diagrammatic expansion of correlation functions*

2.3.1. *Definitions and procedure*

We define the two-, three-, four- and n-point correlators in $\boldsymbol{q} = (\boldsymbol{k}, \omega)$ space as

$$\left.\begin{aligned}(2\pi)^{d+1}\delta(\boldsymbol{q}_1+\boldsymbol{q}_2)\,{}^{2}\mathcal{F}(\boldsymbol{q}_1,\boldsymbol{q}_2) &= \frac{\langle a_{\boldsymbol{q}_1} a_{\boldsymbol{q}_2}\rangle}{2!},\\ (2\pi)^{d+1}\delta(\boldsymbol{q}_1+\boldsymbol{q}_2+\boldsymbol{q}_3)\,{}^{3}\mathcal{F}(\boldsymbol{q}_1,\boldsymbol{q}_2,\boldsymbol{q}_3) &= \frac{\langle a_{\boldsymbol{q}_1} a_{\boldsymbol{q}_2} a_{\boldsymbol{q}_3}\rangle}{3!},\end{aligned}\right\} \tag{2.10a}$$

$$(2\pi)^{d+1}\delta(\boldsymbol{q}_1+\boldsymbol{q}_2+\boldsymbol{q}_3+\boldsymbol{q}_4)\,{}^{4}\mathcal{F}(\boldsymbol{q}_1,\boldsymbol{q}_2,\boldsymbol{q}_3,\boldsymbol{q}_4) = \langle a_{\boldsymbol{q}_1} a_{\boldsymbol{q}_2} a_{\boldsymbol{q}_3} a_{\boldsymbol{q}_4}\rangle/(4!), \tag{2.10b}$$

$$\left.\begin{aligned}(2\pi)^{d+1}\delta\left(\sum_{j=1}^{n}\boldsymbol{q}_j\right)\,{}^{n}\mathcal{F}(\boldsymbol{q}_1,\ldots,\boldsymbol{q}_n) &\equiv \left\langle \prod_{j=1}^{n} a_{\boldsymbol{q}_j}\right\rangle/(n!), \quad n=2,3,\ldots,\\ {}^{2}\mathcal{F}(\boldsymbol{q}) &\equiv {}^{2}\mathcal{F}(\boldsymbol{q},-\boldsymbol{q}).\end{aligned}\right\} \tag{2.10c}$$

Here, d is the dimension of space. In the case of 2-D turbulence, $d = 2$. We have included prefactor $1/n!$ in the definition (2.10) of n-point correlation function ${}^{n}\mathcal{F}$. Note that $n!$ is the number of elements of the symmetry group of a correlator, which is equal to the

number of permutations in the definition of ${}^{n}\mathcal{F}$ in the definition (2.10*a*). This is precisely the choice that ensures the applicability of our $1/N$ symmetry rule for the correlation functions. As we will see below, this particular choice simplifies the appearance of final expressions for ${}^{n}\mathcal{F}$. Notice that the notation ${}^{2}\mathcal{F}(\boldsymbol{q}, \boldsymbol{q}')$ involves two arguments, while actually, it depends on only one argument, say $\boldsymbol{q}$. Therefore, in (2.10*c*), we define it in the more traditional way.

Diagrammatic presentations of ${}^{2}\mathcal{F}$, ${}^{3}\mathcal{F}$ and ${}^{4}\mathcal{F}$ can be obtained by gluing together two, three and four trees. The gluing is a graphical representation of the averaging over the ensemble of the random force. On the corresponding diagrams of two glued trees, the dashed line crossing out the double correlator is the point where the 'branches' of two trees were 'glued' to form a double correlator. The number of possible combinations of the glued trees will be of crucial importance in further investigation of the diagrammatic series.

For the Gaussian process, the high-order correlation functions can be presented as a product of all possible second-order correlators. Specifically, this means that

$$\langle a_k^* a_l^* a_p a_n \rangle = \mathcal{F}_k \mathcal{F}_l (\delta_p^k \delta_n^l + \delta_n^k \delta_p^l), \quad \langle a_k^* a_l a_p a_n \rangle = 0, \quad \langle a_k a_l a_p a_n \rangle = 0. \qquad (2.11a\text{–}c)$$

In this paper, the n-point correlators ${}^{n}\mathcal{F}$ also will be classified by the number m of interacting vortices in the diagrams, shown as superscript on the right: ${}^{n}\mathcal{F}^{m}$. Thus the lowest and next to lowest diagrams for ${}^{3}\mathcal{F}$ and ${}^{4}\mathcal{F}$ are denoted as ${}^{3}\mathcal{F}^{I}$, ${}^{3}\mathcal{F}^{III}$ and ${}^{4}\mathcal{F}^{II}$, ${}^{4}\mathcal{F}^{IV}$. We will see that the numerical prefactors before the diagrams play a critical role in the triangular re-summation.

2.3.2. *Rules for reading diagrams*

Rules for writing down the analytical expressions corresponding to specific diagrams are pretty universal across different diagrammatic techniques (L'vov & Procaccia 1995). We focus first on reading the diagram in the $(\boldsymbol{r}, t)$ representation. The rules are as follows.

(i) A diagram is a set of lines connected by three-way junctions. Each junction represents an interaction amplitude V (solid dot in figure 1). The wavy lines are the double correlators ${}^{2}\mathcal{F}$, while the wavy–straight lines represent the Green's functions $\mathcal{G}$.

(ii) Each propagator is a function of two sets of arguments, say $\boldsymbol{r}_1, t_1$ and $\boldsymbol{r}_2, t_2$, associated with its ends. In the stationary and space-homogeneous case considered in this paper, the propagators depend only on differences of these arguments, e.g. $\mathcal{G}(\boldsymbol{r}_1 - \boldsymbol{r}_2, t_1 - t_2)$.

(iii) Double correlator ${}^{2}\mathcal{F}(\boldsymbol{r}_1 - \boldsymbol{r}_2, t_1 - t_2)$ is an even function of its arguments. The Green's function measures the response of the velocity field (denoted by a wavy line) to the forcing (denoted by a straight line). Therefore, the Green's function has the inherent time direction dictated by the causality principle. The direction is from the forcing to the velocity field, or from the straight to the wavy line. Consequently, in the Green's function $\mathcal{G}(\boldsymbol{r}_1 - \boldsymbol{r}_2, t_1 - t_2) = 0$ if t_2 (associated with the forcing) is larger than t_1, the value of this Green's function is zero: $\mathcal{G}(\boldsymbol{r}, t) = 0$ if $t < 0$. This a consequence of the causality principle: a response of the velocity $\delta v(t_1)$ to the force $\delta f(t_2)$ must vanish if $t_2 > t_1$.

(iv) Each vertex also has space–time arguments, say $\boldsymbol{r}_n, t_n$, the same as the legs of three propagators connected to it. In the diagram, one has to integrate over arguments $\boldsymbol{r}_n, t_n$ of all inner vertices.

(v) Since each vertex has its own time, we can partition the diagram into time zones. The boundaries of these time zones are denoted by dashed lines in the diagrams, as in figure 8. These time zones will play a significant role in calculating time integrals corresponding to each diagram, as discussed in § 3.

(vi) In e $(\boldsymbol{k},\omega)$ representation, each propagator, say $\mathcal{G}(\boldsymbol{k},\omega)$ (the Fourier image of $\mathcal{G}(\boldsymbol{r},t)$), has only one set of arguments, and each vertex involves delta functions of the sum of $\boldsymbol{k}_n$, ω_n arguments $(2\pi)^{(d+1)}\,\delta(\boldsymbol{k}_1+\boldsymbol{k}_2+\boldsymbol{k}_3)\,\delta(\omega_1+\omega_2+\omega_3)$, where d is the dimensionality of $\boldsymbol{k}$-space. Finally, one has to integrate $\int \mathrm{d}\omega_n/(2\pi)$ and $\int \mathrm{d}\boldsymbol{k}_n/(2\pi)^d$ for all intrinsic lines.

We will use these rules to write down analytical expressions for all the diagrams that we consider below.

2.3.3. *Third-order correlator ${}^3\mathcal{F}^I$ and ${}^3\mathcal{F}^{III}$*

We consider first-order diagrams for triple correlator ${}^3\mathcal{F}^1$. Its first representative ${}^3\mathcal{F}^{1A}_{123}$ is shown in figure 3(*a*) as a diagram ${}^1\mathcal{A}_{1,23}$. From definition (2.10*a*), one gets

$$\left.\begin{gathered}(2\pi)^{d+1}\delta_{123}\,{}^3\mathcal{F}^{1A}_{123}=\underset{123}{\boldsymbol{P}}\,{}^1\mathcal{A}_{1,23},\quad (2\pi)^{d+1}\delta_{123}\,{}^1\mathcal{A}_{1,23}=\tfrac{1}{2}\langle a_1^1 a_2 a_3\rangle,\\ \delta_{123}\equiv\delta(\boldsymbol{q}_1+\boldsymbol{q}_2+\boldsymbol{q}_3).\end{gathered}\right\}\tag{2.12a}$$

Here, $\underset{123}{\boldsymbol{P}}$ is the permutation operator that, when acting on the function, produces a sum of all possible permutations of its indices divided by the number of all possible permutations of the indices. For example, $\underset{123}{\boldsymbol{P}}\mathcal{A}_{1,23}\equiv\frac{1}{3!}(\mathcal{A}_{1,23}+\mathcal{A}_{1,32}+\mathcal{A}_{2,13}+\mathcal{A}_{2,31}+\mathcal{A}_{3,12}+\mathcal{A}_{3,21})$. Substituting ${}^1a_1$ from (2.8*a*) into ${}^1\mathcal{A}_{1,23}$, one gets ${}^1\mathcal{A}_{1,23}=\frac{1}{4}\mathcal{G}_1V_{156}\langle a_5a_6a_2a_3\rangle$. Hereafter, we colour in blue parts originating from the tree ${}^1a_{\boldsymbol{q}}$ in (A16*a*). We now average the resulting expression using the pairing rule (2.11*a–c*), which corresponds to gluing together the trees of ${}^1a_{\boldsymbol{q}}$ and $a_{\boldsymbol{q}}$. The result is pairs $\overbrace{a_5\,a_6}$ and $\overbrace{a_2\,a_3}$ that give uncoupled contributions (each of them is equal to zero). Two equivalent ways to pair $\overbrace{a_5\,a_2}$ and $\overbrace{a_5\,a_3}$ (denoted for the brevity as $\overbrace{5\text{-}2}$ and $\overbrace{5\text{-}3}$, or even more briefly as $[\overbrace{5\text{-}(2}, 3)]$) result in

$${}^1\mathcal{A}_{1,23}=\tfrac{1}{2}\mathcal{G}_1V_{123}\mathcal{F}_2\mathcal{F}_3.\tag{2.12b}$$

Graphically, this result is shown in figure 3(*a*). We preserve the notation ${}^n\mathcal{A}_{1,2\ldots}$ for all diagrams of nth order in vertices V with one leg denoting the Green's function $\mathcal{G}_1$ and any number of wavy tails denoting $\mathcal{F}_j$. Here and in the rest of the paper, we separate by a comma the indices in the correlators corresponding to the Green's functions from those corresponding to the double correlators.

For third-order diagrams for triple correlator ${}^3\mathcal{F}^3$, we compute the three-point correlator in the third order in the interaction vertex. As we will show below, this object plays a key role in the statistical properties of hydrodynamic turbulence. This object appears as a result of gluing together three trees and leads to the diagrams that are triangular in shape.

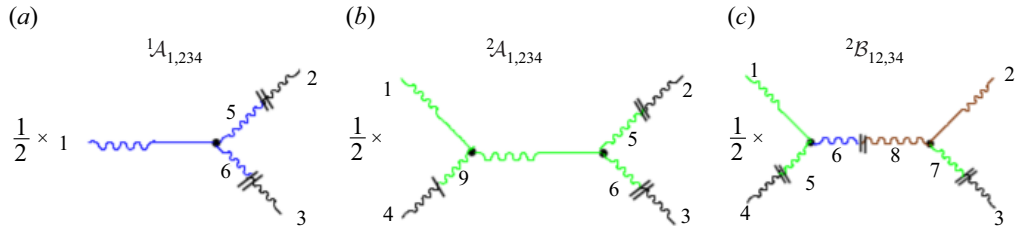

Figure 3. The lowest-order contributions to (*a*) the three-point correlator ${}^3\mathcal{F}^{1A}_{123}$ and (*b*,*c*) the four-point correlator ${}^3\mathcal{F}^{2A}_{1234}$ and ${}^3\mathcal{F}^{2B}_{1234}$ as a result of gluing of three and four trees, separated by ‖. All diagrams include prefactors. The operator $\boldsymbol{P}$ is not shown explicitly on this and subsequent diagrams, but its presence is implied.

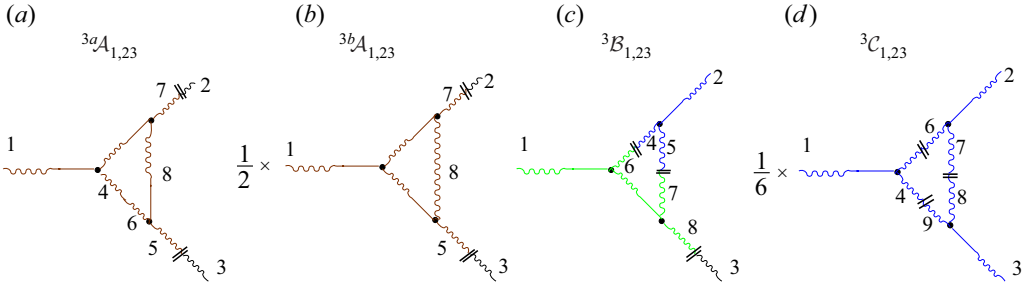

Figure 4. Triangular diagrams for the next-lowest third-order triple correlation function as a result of gluing three trees, separated by ‖. Diagrams with one, two and three Green's function in the legs are denoted as $\mathcal{A}$, $\mathcal{B}$ and $\mathcal{C}$. All diagrams include prefactors according to the $1/N$ symmetry rule.

To calculate ${}^3\mathcal{F}^3$, we use (2.10*a*) and collect all terms $\propto V^3$:

$$\left.\begin{gathered}(2\pi)^{d+1}\delta^{d+1}_{123}\,{}^3\mathcal{F}^{(3)}_{123} = \underset{123}{\boldsymbol{P}}[{}^{3a}\mathcal{A}_{1,23} + {}^{3b}\mathcal{A}_{1,23} + {}^3\mathcal{B}_{12,3} + {}^3\mathcal{C}_{123}],\\ {}^{3a}\mathcal{A}_{1,23} = \langle {}^{3a}a_1a_2a_3\rangle/2, \quad {}^{3b}\mathcal{A}_{1,23} = \langle {}^{3b}a_1a_2a_3\rangle/2,\\ {}^3\mathcal{B}_{12,3} = \langle a_1^2a_2^1a_3\rangle, \quad {}^3\mathcal{C}_{123} = \langle a_1^1a_2^1a_3^1\rangle/3!.\end{gathered}\right\} \tag{2.13}$$

These terms are computed in § A.1, and the results are given by

$${}^{3a}\mathcal{A}_{1,23} = \mathcal{G}_1\mathcal{F}_2\mathcal{F}_3\int\frac{\mathrm{d}\boldsymbol{q}_4}{(2\pi)^{d+1}}\,V_{14\overline{1+4}}V_{\bar4(4-2)2}V_{(2-4)3(1+4)}\mathcal{G}^*_4\mathcal{G}_{2-4}\mathcal{F}_{1+4}, \tag{2.14a}$$

$${}^{3b}\mathcal{A}_{1,23} = \frac{1}{2}\mathcal{G}_1\mathcal{F}_2\mathcal{F}_3\int\frac{\mathrm{d}\boldsymbol{q}_4}{(2\pi)^{d+1}}\,\mathcal{G}^*_4\mathcal{F}_{2-4}\mathcal{G}_{1+4}V_{14\overline{(1+4)}}V_{\bar4(4-2)2}V_{(4+1)3(2-4)}, \tag{2.14b}$$

$${}^3\mathcal{B}_{12,3} = \mathcal{G}_1\mathcal{G}_2\mathcal{F}_3\int\frac{\mathrm{d}\boldsymbol{q}_4}{(2\pi)^{d+1}}\,\mathcal{F}_4\mathcal{F}_{4-2}\mathcal{G}_{1+4}V_{14\overline{(1+4)}}V_{2\bar4(4-2)}V_{(4+1)3(2-4)}, \tag{2.14c}$$

$${}^3\mathcal{C}_{123} = \frac{1}{6}\mathcal{G}_1\mathcal{G}_2\mathcal{G}_3\int\frac{\mathrm{d}\boldsymbol{q}_4}{(2\pi)^{d+1}}\,\mathcal{F}_4\mathcal{F}_{4-2}\mathcal{F}_{1+4}V_{14\overline{(1+4)}}V_{2\bar4(4-2)}V_{3(1+4)(2-4)}. \tag{2.14d}$$

Recall that an overline over indices indicates the negative of the corresponding wave vector, and the sums of indices imply the sum of corresponding wavenumbers, e.g. $V_{14\overline{(1+4)}} \equiv V_{k_1,k_4,-k_1-k_4}$. The corresponding diagrams are shown in figures 4(*a–d*).

2.3.4. *Four-point correlation function*

Second-order diagrams for ${}^4\mathcal{F}^{(2)}$ are proportional to the product of two vertices V. They originates from ten terms, which we divide into two groups ${}^2\mathcal{A}_{1,234}$ with one and two G-tails involving Green's functions. Hereafter, we preserve the notation ${}^n\mathcal{B}_{12,\dots}$ for all diagrams of nth order in V with two legs $\mathcal{G}_1$, $\mathcal{G}_2$ and any number of wavy tails denoting $\mathcal{F}_j$. As before, we separate by a comma the indices in the correlators corresponding to the Green's functions from those from the correlators. The resulting analytical expressions for the four-point correlator are given by

$$\left.\begin{aligned}(2\pi)^{d+1}\delta_{1234}\,{}^4\mathcal{F}^{(2)}_{1234} &= \boldsymbol{P}_{1234}[{}^2\mathcal{A}_{1,234}+{}^2\mathcal{B}_{12,34}],\\ {}^2\mathcal{A}_{1,234} = \langle {}^2a_1a_2a_3a_4\rangle/3!,&\quad {}^2\mathcal{B}_{12,34} = \langle {}^1a_1\,{}^1a_2a_3a_4\rangle/4.\end{aligned}\right\} \tag{2.15}$$

The required pairings are presented in § A.2. The results are diagrams in figures 3(*b*,*c*) with

$$\left.\begin{aligned}{}^2\mathcal{A}_{1,234} &= \tfrac{1}{2}\mathcal{G}_1\mathcal{G}_5V_{145}V_{523}\mathcal{F}_2\mathcal{F}_3\mathcal{F}_4,\\ {}^2\mathcal{B}_{12,34} &= \tfrac{1}{2}\mathcal{G}_1\mathcal{G}_2\mathcal{F}_3\mathcal{F}_4\mathcal{F}_5V_{135}V_{235},\quad \boldsymbol{q}_5=(\boldsymbol{q}_1+\boldsymbol{q}_4).\end{aligned}\right\} \tag{2.16}$$

These results will be used to obtain a single-time version of the four-point correlator in the second order in the interaction vertex.

Fourth-order diagrams for ${}^4\mathcal{F}^{(4)}_{1234}\propto V^4$ have seven types of terms:

$$\left.\begin{aligned}(2\pi)^4\delta_{1234}\,{}^4\mathcal{F}^{(4)}_{1234} &= \boldsymbol{P}_{1234}\{{}^{4a}\mathcal{A}_{1,234}+{}^{4b}\mathcal{A}_{1,234}+{}^{4a}\mathcal{B}_{1234}\\ &\quad+{}^{4b}\mathcal{B}_{1234}+{}^{4c}\mathcal{B}_{1234}+{}^4\mathcal{C}_{1234}+{}^4\mathcal{D}_{1234}\},\\ {}^{4a}\mathcal{A}_{1,234} &= \frac{\langle {}^{4a}a_1a_2a_3a_4\rangle}{3!},\quad {}^{4b}\mathcal{A}_{1,234} = \frac{\langle {}^{4b}a_1a_2a_3a_4\rangle}{3!},\\ {}^{4a}\mathcal{B}_{12,34} &= \frac{\langle {}^{3a}a_1\,{}^1a_2a_3a_4\rangle}{2},\quad {}^{4b}\mathcal{B}_{12,34} = \frac{\langle {}^{3b}a_1\,{}^1a_2a_3a_4\rangle}{2},\\ {}^{4c}\mathcal{B}_{1234} &= \frac{\langle {}^2a_1\,{}^2a_2a_3a_4\rangle}{4},\quad {}^4\mathcal{C}_{123,4} = \frac{\langle {}^2a_1\,{}^1a_2\,{}^1a_3a_4\rangle}{2},\quad {}^4\mathcal{D}_{1234} = \frac{\langle {}^1a_1\,{}^1a_2\,{}^1a_3\,{}^1a_4\rangle}{4!}.\end{aligned}\right\} \tag{2.17}$$

The resulting diagrams and corresponding analytical expressions are computed in § A.3. The diagrams are shown in figure 5, while the corresponding analytical expressions are given by (A16).

2.4. *Diagrammatic rules for plotting high-order correlation functions*

Examining diagrams in figure 2 for the velocity field $a_{\boldsymbol{q}}$, we see that it is possible to write the nth-order diagrams for $a_{\boldsymbol{q}}$ without going through the cumbersome analytic substitutions presented by (2.8): the diagrams corresponding to the velocity field $a_{\boldsymbol{q}}$ are given by all topologically distinct binary trees with n vertices, such that all the trunks are made of Green's functions, and all the end branches are made of $a_{\boldsymbol{q}}$ terms. Furthermore, every portion of the tree that continues in a symmetric fashion gets a factor $1/2$ due to the symmetry of the original equation of motion. Therefore, the overall numerical prefactor for a tree with N elements in its symmetry group is $1/N$.

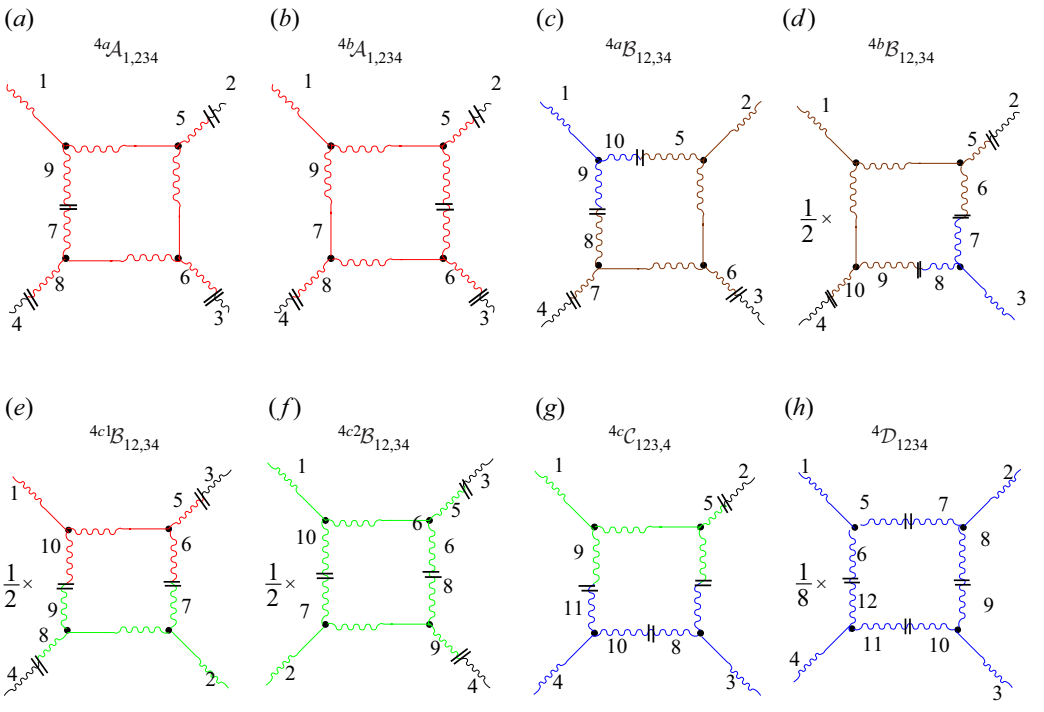

Figure 5. The fourth-order 'square' diagrams for the quadruple correlation function $^{4}\mathcal{F}^{(4)}_{1234}$ as result of gluing of four trees, separated by $\|$. Corresponding analytical expressions are presented in (A16). Diagrams with one, two, three and four Green's functions in the legs are denoted as $\mathcal{A}$, $\mathcal{B}$, $\mathcal{C}$ and $\mathcal{D}$. All diagrams include the symmetry prefactor $1/N$.

Examining figures 3–5 for the diagrams for $^{3}\mathcal{F}$ and $^{4}\mathcal{F}$, we formulate the rules of the diagrammatic technique, which allows us to skip the procedure of step-by-step derivation by gluing corresponding trees.

(i) Diagrams for the n-point, mth-order correlator $^{n}\mathcal{F}^{(m)}$ are all topologically different graphs with m vertices and n external wavy tails. These wavy tails are either the Green's functions $\mathcal{G}$, or double correlations $\mathcal{F}$.
(ii) Each vertex in the diagram can be reached in only one way via $\mathcal{G}$ from the outer leg of $\mathcal{G}$.
(iii) There are no loops made of the $\mathcal{G}$ functions.
(iv) According to our $1/N$ symmetry rule, the prefactor for a diagram with N elements in its symmetry group is $1/N$.

In particular, diagrams without any symmetry (i.e. with only $N = 1$ element of symmetry), including diagrams in figures 3(*b*), 4(*a*,*c*) and 5(*a*,*b*,*c*,*e*,*g*), have numerical prefactor equal to unity. Furthermore, the diagrams with non-trivial symmetry element (i.e. $N = 2$) have prefactor 1/2, as in the diagram $^{1}\mathcal{A}_{1,23}$ with the symmetry $2 \Leftrightarrow 3$ in figure 3(*a*), diagram $^{2}\mathcal{B}_{12,34}$ with the symmetry $1 \Leftrightarrow 2$ together with $3 \Leftrightarrow 4$ in figure 3(*c*), diagram $^{3b}\mathcal{A}_{1,23}$ with the symmetry $2 \Leftrightarrow 3$ in figure 4(*b*), and so on. The most symmetrical ones are the diagram for $^{3}\mathcal{C}_{123}$ in figure 4(*d*) (symmetrical under permutations of all three arguments) with $P = 3! = 6$, which generates prefactor 1/6, and the diagram for $^{4}\mathcal{D}_{1234}$

in figure 5(*h*), which is symmetrical under reflection in four lines – horizontal, vertical, and 1–3 and 2–4 oblique lines – and rotation by the angles $\phi = 0, \pi/2, \pi, 3\pi/2$. Thus for the ${}^4\mathcal{D}_{1234}$ diagram, $N = 8$ and the $1/N$ prefactor is equal to $1/8$.

Analyses of these diagrams and a wide set of additional diagrams not presented here demonstrate that the above-formulated diagrammatic rules work not only for the diagrams as a whole but also for their fragments. So we expect that this is the general rule for diagrams for all orders and for all of a diagram's fragments.

We think that this fact follows from the internal structure of the presented perturbation theory, reflected in the topology of diagrams. Bearing in mind that the question of the numerical prefactor is of principal importance, allowing triangular re-summation of high-order diagrams, and that its rigorous mathematical proof is still absent, we decided to check it constructively for all diagrams considered in this paper.

3. Simultaneous correlation functions

In this section, we show how and why the simultaneous correlators can be further re-summed up to powers of the simultaneous triple correlator ${}^3F$. As a preliminary step, we introduce all required simultaneous correlations in the $\boldsymbol{k}$-space: $F(\kappa) \equiv F_\kappa$, ${}^3F(\kappa_1, \kappa_2, \kappa_3) \equiv {}^3F_{123}$ and ${}^4F(\kappa_1, \kappa_2, \kappa_3, \kappa_4) \equiv F_{1234}$, where $(2\pi)^d \delta(\kappa_1 + \kappa_2) F(\kappa_1) \equiv \langle a_{\kappa_1} a_{\kappa_2} \rangle$, $(2\pi)^d \delta(\kappa_1 + \kappa_2 + \kappa_3)\, {}^3F_{123} \equiv \langle a_{\kappa_1} a_{\kappa_2} a_{\kappa_3} \rangle / (3!)$, $(2\pi)^d \delta(\kappa_1 + \kappa_2 + \kappa_3 + \kappa_4)\, {}^4F_{1234} \equiv \langle a_{\kappa_1} a_{\kappa_2} a_{\kappa_3} a_{\kappa_4} \rangle / (4!)$, etc. The simultaneous correlation functions relate to different-time correlators in the $\boldsymbol{q} = (\kappa, \omega)$ representation as follows:

$$\left.\begin{aligned} F(\kappa) &= \int \frac{\mathrm{d}\omega}{2\pi}\, \mathcal{F}(\kappa, \omega), \\ {}^3F(\kappa_1, \kappa_2, \kappa_3) &= \int \frac{\mathrm{d}\omega_1\, \mathrm{d}\omega_2\, \mathrm{d}\omega_3}{(2\pi)^d}\, {}^3\mathcal{F}(\boldsymbol{q}_1, \boldsymbol{q}_2, \boldsymbol{q}_3)\, \delta(\omega_1 + \omega_2 + \omega_3), \end{aligned}\right\} \tag{3.1a}$$

$${}^4F(\kappa_1, \kappa_2, \kappa_3, \kappa_4) = \int \frac{\mathrm{d}\omega_1\, \mathrm{d}\omega_2\, \mathrm{d}\omega_3\, \mathrm{d}\omega_4}{(2\pi)^{d+1}}\, \delta(\omega_1 + \omega_2 + \omega_3 + \omega_4)\, {}^4\mathcal{F}(\boldsymbol{q}_1, \boldsymbol{q}_2, \boldsymbol{q}_3, \boldsymbol{q}_4). \tag{3.1b}$$

Therefore, to obtain a single-time correlator of any order, the corresponding multiple time correlator needs to be multiplied by the delta function of the sum of all the frequencies and then integrated over all frequencies.

3.1. *One-pole approximation*

For the actual calculation of integrals in (3.1), one needs to know the ω dependence of $G(\kappa, \omega)$ and $\mathcal{F}(\kappa, \omega)$. Therefore, to proceed further, we adopt the so-called one-pole approximation (L'vov, Lvov & Pomyalov 2000) in which the ω dependence of the 'mass operator' $\Sigma_{\boldsymbol{k},\omega}$ in (2.9) for the Green's function $\mathcal{G}_{\boldsymbol{q}}$ is neglected. Similarly, we further neglect ω dependence of the mass operator $\Phi_{\kappa,\omega} \Rightarrow \Phi_\kappa$ in Wyld's equation for $\mathcal{F}_{\boldsymbol{q}} = |G_{\boldsymbol{q}}|^2 (\Phi_{\boldsymbol{q}} + D_{\boldsymbol{q}})$, where $D_{\boldsymbol{q}}$ is a correlator of the white noise. Furthermore, in the Dyson equation, we neglect the double correlator of the white noise, since it is much smaller than $\Phi_{\boldsymbol{q}}$. As a result, we have

$$G_{\kappa,\omega} = \frac{\mathrm{i}}{\omega + \mathrm{i}\gamma_k}, \quad \mathcal{F}_{\kappa,\omega} = \frac{\Phi_\kappa}{\omega^2 + \gamma_k^2} = \frac{2\gamma_k F_\kappa}{\omega^2 + \gamma^2} = 2\,\mathrm{Re}\{G_{\kappa,\omega}\} F_\kappa. \tag{3.2}$$

Equations (3.2) replace $\mathcal{F}_{\kappa,\omega}$ by the sum of the Green's function and its complex conjugate multiplied by F_κ. This replacement is the crucial step that enables us to group diagrams in the triads that form the simultaneous triple correlator ${}^3F_{\cdot\cdot}$. We denote $\tilde{\mathcal{G}}_{\boldsymbol{q}} \equiv \mathcal{G}_{\boldsymbol{q}} F_\kappa$ as an 'auxiliary Green's function', while the original Green's function $G_{\boldsymbol{q}}$ is called the 'true' Green's function. To distinguish between 'true' and 'auxiliary' Green's functions in the diagrammatic series, the auxiliary Green's functions will be distinguished by an additional 'dash' crossing a line. The diagrams with the double correlator will be called 'parent' diagrams. The diagrams that are generated by replacing the double correlator with the two auxiliary Green's functions will be called 'child diagrams', or 'children' for short.

The diagrams with the loop along Green's functions with the same orientation give zero contribution to ${}^nF_{\cdots}$ due to the causality principle. This is true regardless of whether the Green's function is 'true' or auxiliary. This property can be seen in the t or ω representation. In the t representation, we should recognize that the wavy tail of each Green's function has time t_w, while the straight tail has time $t_s > t_w$. Otherwise, the Green's function is zero due to the causality principle. Therefore the wavy tail of the Green's function in the next loop will have time $t_{w,n+1}$, even earlier than $t_{w,n}$. Such Green's functions will vanish. Consequently, the value of all loops with the same orientation of the Green's functions vanishes, thus the diagrams with loops in the Green's functions with the same orientation may be omitted from the very beginning.

The same conclusion can be obtained in the ω representation: similarly oriented number n Green's functions with frequencies ω_1, $\omega_2 = \omega_1 + \delta_1$, $\omega_3 = \omega_1 + \delta_1 + \delta_2$, etc. (here, δ_n is the 'incoming' frequency from the connected line in the nth vertex) are analytical in some ω_1 half-plane, again as a consequence of the causality principle. Therefore, the ω_1 frequency integral in the loop indeed vanishes. Similarly, it is possible to show that diagrams involving a chain of similarly oriented Green's function connected to any of external tails do not contribute to the simultaneous correlators ${}^nF_{\cdots}$ as a manifestation of the causality principle. This statement is again true regardless of whether the Green's function is 'true' or 'auxiliary'.

3.2. *Time zones and interaction time integrals in the diagrams for* ${}^3F_{123}$ *and* ${}^4F_{1234}$

In this subsection, we consider the actual procedure for calculations of integrals for interaction times, of the type presented in (3.1), in the one-pole approximation. Below, we begin with the simplest case of diagrams for ${}^3F^{(1)}$.

3.2.1. *First-order triad for* ${}^3F^I_{123}$

After replacement of (3.2) in (2.12*b*), we obtain three diagrams for ${}^1F^{(3)}_{123}$, shown in figure 6. Two of them, shown in figures 6(*c*,*d*), vanish after frequency integrations, as required by (3.1*a*). A non-zero diagram in figure 6(*b*) under the permutation operator $\boldsymbol{P}_{123}$ in (2.12*a*) can be presented as the sum of three diagrams, shown in figures 6(*e*–*g*). The set of these three diagrams that are symmetric with respect to the permutation of their legs, oriented inside with the straight line, will be referred to below as a 'triad'. The simplest triad with only one vertex inside, as shown in figure 6, will be called a first-order triad. As we see, this is nothing but the diagram for ${}^1F^{(3)}_{123}$ shown in figure 6(*a*) as a thin red triangle.

Analytically, diagrams for ${}^3F^I_{123}$ are as follows:

$$ {}^3F^I_{123} = \underset{123}{\boldsymbol{P}}\, {}^1A_{1,23}, \quad {}^1A_{1,23} = \tfrac{1}{2} T_{123} V_{123} F_2 F_3, \quad \boldsymbol{q}_1 + \boldsymbol{q}_2 + \boldsymbol{q}_3 = 0, \qquad (3.3a\text{–}c) $$

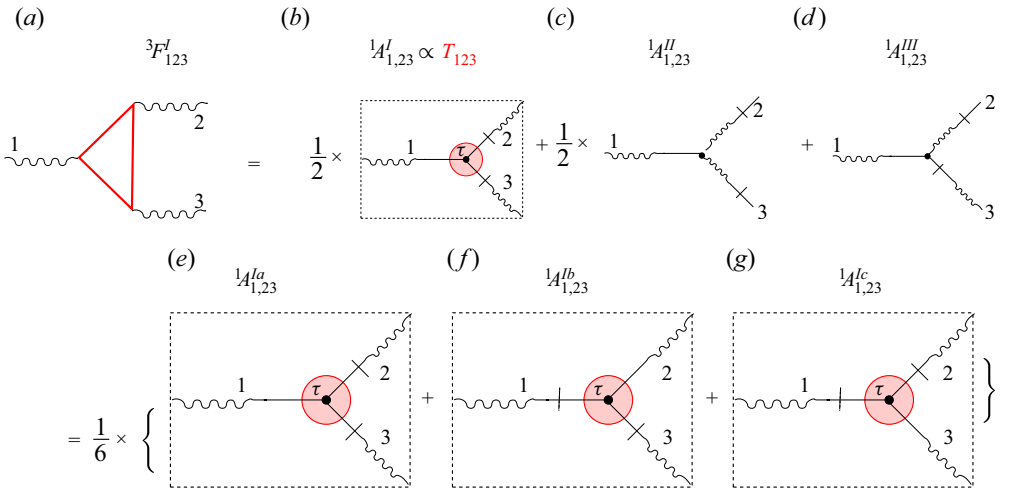

Figure 6. The lowest (first) order triple correlator ${}^1F_{123}$ shown in (*a*) as a thin red triangle, and its 'child' diagrams ${}^1\mathcal{A}_{1,23} \propto^3 T_{123}$ shown in (*b*,*c*,*d*). These child diagrams originated from ${}^1\mathcal{A}_{1,23}$ shown in figure 3(*a*). Only the first of them, ${}^1A^I_{1,23}$, shown in (*b*), survives in simultaneous correlator ${}^1A_{1,23}$, proportional to the frequency integral I_1; see (3.4*c*). (*e*,*f*,*g*) with cycling relabeling of the legs 1, 2 and 3 present the diagram in (*a*). The dashed line connecting the wavy legs of the Green's functions stands for the present time border: $t_1 = t_2 = t_3 = 0$. All times inside this region belong to the past, $t < 0$. The filled red circle represents the time zone $\tau < 0$ in this plot.

where we introduced the triad interaction time

$$T_{123} = \int \mathrm{d}\omega_1\, \mathrm{d}\omega_2\, \mathrm{d}\omega_3\, G_1 G_2 G_3\, \delta(\omega_1 + \omega_2 + \omega_3)/(2\pi)^d. \tag{3.4a}$$

In the one-pole approximation (3.2), this integral can be taken easily to obtain

$$T_{ijk} \equiv 1/(\gamma_i + \gamma_j + \gamma_k), \quad \gamma_i \equiv \gamma(k_i),\ \gamma_j \equiv \gamma(k_j), \ldots. \tag{3.4b}$$

Applying the $\boldsymbol{P}_{123}$ operation in (3.3*a–c*) and substituting (3.4*a*), we obtain

$${}^3F^I_{123} = \frac{V_{123}F_2F_3 + V_{231}F_1F_3 + V_{321}F_2F_3}{6(\gamma_i + \gamma_j + \gamma_k)}. \tag{3.5}$$

It was shown in L'vov *et al.* (2002) that the fractional dimension of $d = 4/3$, the scaling index of the inverse cascade of energy $F_k \propto 1/k^2$, coincides with the scaling index of the thermodynamical equilibrium with the equipartition of enstrophy. In this case, the expression in the numerator of the right-hand side of (3.5) vanishes due to the second Jacobi identity in (2.4*a*,*b*). Consequently, the value of the simultaneous triple correlator in the first order vanishes for the inverse cascade of the energy in the fractional dimension of $d = 4/3$. It was argued in L'vov *et al.* (2002) that this is the reason why the statistics of 2-D turbulence is close to Gaussian.

We will see below that ω integral (3.4*a*) and much more complicated ω integrals are much easier to calculate in the $(\boldsymbol{k}, t)$ representation. To translate any diagram to the $(\boldsymbol{k}, t)$ representation, we assign different times to the beginning and end of each Green's function: $G_i \equiv G(\boldsymbol{k}, \tau - t_j)$, $j = 1, 2, 3$. In the one-pole approximation, Green's function

(3.2) has the form

$$G(\boldsymbol{k}, \tau) = \exp(\gamma_k \tau) \text{ for } \tau < 0, \text{ and zero otherwise;} \tag{3.6}$$

the Green's functions are equal to zero for positive times as the future cannot affect the present (the causality principle).

Now consider the diagrams in figures 6(*e–g*). Since this is a one-time correlator, the external ends should have equal times assigned. Let us assign the time to be zero, as in $t_1 = t_2 = t_3 = 0$, and connect them by the dotted line 'present time-border', which separates the future (outside the diagram) and past (inside the diagram) time intervals. The time of the vertex τ belongs to the past and goes from $-\infty$ to zero. Now integral (3.4*a*) in the $(\boldsymbol{k}, t)$ representation can be written as

$$\begin{aligned} T_{123} &= \int_{-\infty}^{0} \mathrm{d}\tau \, G(\boldsymbol{k}_1, \tau) \, G(\boldsymbol{k}_2, \tau) \, G(\boldsymbol{k}_3, \tau) \\ &= \int_{-\infty}^{0} \exp\left[(\gamma_1 + \gamma_2 + \gamma_3)\tau\right] \mathrm{d}\tau = 1/(\gamma_1 + \gamma_2 + \gamma_3). \end{aligned} \tag{3.7}$$

The answers (3.4*a*) and (3.7) for the triple interaction time are equivalent. Naturally, the answer is independent on whether it is obtained in the t or ω representation.

3.2.2. *Third-order triad for* ${}^3F^{III}_{123}$

To calculate the third-order triple correlator ${}^3F^{III}$, we take (3.2) and substitute it into (2.14). Graphically, this corresponds to replacing all three double correlators of ${}^{3a}\mathcal{A}_{1,23}$ by the pair of auxiliary Green's functions, run in either direction (i.e. eight possibilities). The six of the total of $4 \times 8 = 32$ possibilities give non-zero contributions for simultaneous correlation functions. The resulting six diagrams are shown in figure 7, denoted as ${}^{3a}A^{I}_{1,23}$, ${}^{3b}A^{I}_{1,23}$, $B^{I}_{12,3}$, $B^{II}_{12,3}$, $B^{III}_{12,3}$ and $C^{I}_{1,23}$ and the corresponding analytical expressions are (B1)–(B3) given in Appendix B.

As explained above, Green's functions have an inherent time direction in corresponding diagrams: time flows in the direction from a wavy to a straight line. Therefore, the beginning of the Green's function has an earlier time than the end of the Green's function that enters the vertex. To calculate one-time correlators, we replace the double correlator with the sum of the two auxiliary Green's functions oriented in the opposite directions. These Green's functions therefore partition the diagram for a multi-point correlator in the distinct time zones. Making an arbitrary choice that the external legs of the diagram correspond to time $t = 0$, we have earlier times inside the diagram. In fact, we have telescopically nested time zones that flow from the earliest time zone to the present time zone. In our diagrams, we colour the earliest time zone as red, later as green, and even later as blue. We colour the latest time zone, if present, as magenta. The number of nested time zones is equal to the number of interaction vertices. In some diagrams, the ordering of the zones is not defined uniquely by Green's functions. For such diagrams, as explained below and in figure captions, all possible ordering of time zones must be taken into account in calculating interaction time integrals for the simultaneous correlators.

As before, we connect all three external wavy legs of the Green's functions by the black dotted line, denoting the present time border $t_1 = t_2 = t_3 = 0$. The times of three vertices are denoted as τ_1, τ_2 and τ_3 in figure 7(*d*). Each of these times belongs to a particular time zone, coloured red, green or blue.

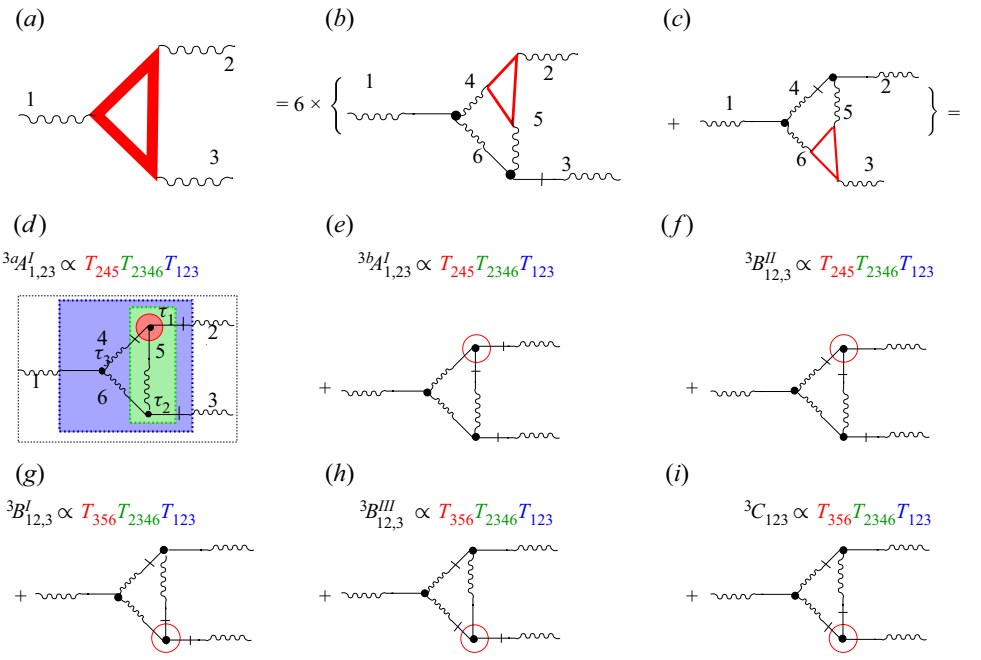

Figure 7. The next lowest order (third-order) 'child' diagrams for the simultaneous triple correlator $^{3}F^{III}_{123}$, denoted in (*a*) as a thick red triangle. (*b*,*c*) Representation via $^{3}F^{I}_{123}$, denoted as thin red triangles, while (*d*–*i*) show original (not summed yet) diagrams for $^{3}F^{III}_{123}$. (*b*) Sum of panels (*d*–*f*). (*c*) Sum of panels (*g*–*i*). Three chronologically nested (red–green–blue) time zones are shown in (*d*), producing the product of three interaction times: factor T_{2346} appears from the integration of $G_2G_3G_4G_6$ over τ_2, etc. These notations are used on all subsequent figures.

According to the causality principle, all of these time zones belong to the past: $\tau_1 < 0$, $\tau_2 < 0$ and $\tau_3 < 0$. The present time depends only on the past time, and does not depend on the future. Green's functions $G(\boldsymbol{k}_4, \tau_{21})$, $G(\boldsymbol{k}_5, \tau_{23})$ and $G(\boldsymbol{k}_6, \tau_{31})$ (hereafter $\tau_{ij} \equiv \tau_i - \tau_j$) in this diagram prescribe the chronological order of the time zones: $\tau_2 < \tau_3 < \tau_1 < 0$.

Armed with this arrangement, we can easily compute the time integral in figure 7(*a*),

$$I_{A1} = \int_{-\infty}^{0} \mathrm{d}\tau_1\, G(\boldsymbol{k}_1, \tau_1) \times \int_{-\infty}^{\tau_1} \mathrm{d}\tau_3\, G(\boldsymbol{k}_3, \tau_3) \times \int_{-\infty}^{\tau_3} \mathrm{d}\tau_2\, G(\boldsymbol{k}_2, \tau_2)\, G(\boldsymbol{k}_4, \tau_2 - \tau_1)\, G(\boldsymbol{k}_5, \tau_2 - \tau_3)\, G(\boldsymbol{k}_6, \tau_3 - \tau_1), \tag{3.8}$$

written in the t representation for figure 8(*a*-i). Most Green's functions, except for $G(\boldsymbol{k}_1, \tau_1)$, cross borders between time zones such that their fragments belong to different zones. Using the decomposition rule $G(\tau) = G(\tau - \tau')G(\tau')$ for the Green's function in the one-pole approximation (3.6), we can present these Green's functions as the product of the Green's functions such that each of them belongs to only one time zone. Namely, $G(\boldsymbol{k}_2, \tau_2) = G(\boldsymbol{k}_2, \tau_{23})\, G(\boldsymbol{k}_2, \tau_{31})\, G(\boldsymbol{k}_2, \tau_1)$, $G(\boldsymbol{k}_3, \tau_3) = G(\boldsymbol{k}_3, \tau_{31})\, G(\boldsymbol{k}_3, \tau_1)$ and $G(\boldsymbol{k}_4, \tau_{21}) = G(\boldsymbol{k}_4, \tau_{23})\, G(\boldsymbol{k}_2, \tau_{31})$. Now interaction time integral I can be factorized

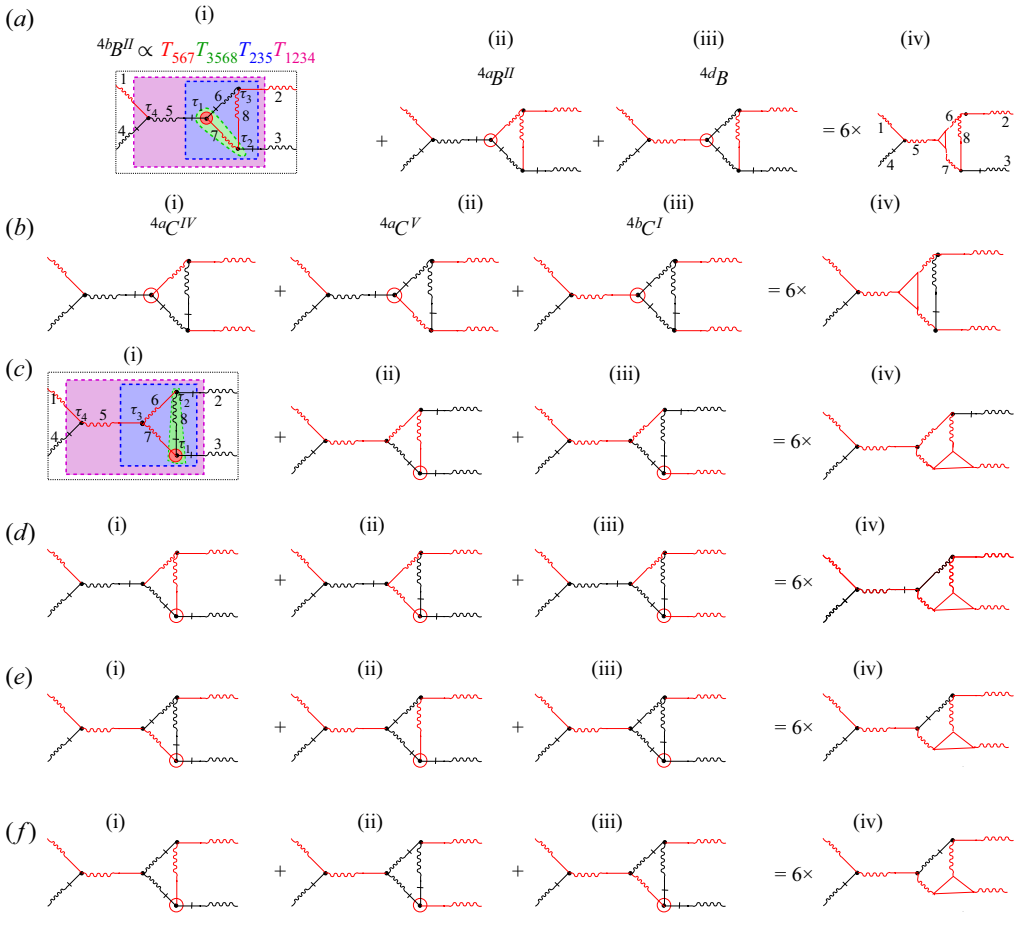

Figure 8. First group of the skeleton diagrams, with the earliest time zones in the (678)-triangle, denoted by a red circle. Similar to figure 7, the time zones are coloured as red–green–blue–magenta from the earliest to the latest time zones. The time factors are coloured according to the time zones they originate from. As in figures 6, 7 and 10, interaction times T appear from the integrations of the product of the Green's functions, entering the appropriate time zone by straight lines, over the time τ_j of their vertex. Therefore there are as many time zones as there are vertices. These time factors are coloured accordingly to the time zones they originate from.

as $I = {}^3T_{123}\,{}^3T_{245}\,{}^4T_{2346}$, where

$$\left.\begin{aligned} T_{123} &= \int_{-\infty}^{0} \mathrm{d}\tau_1\, G(\boldsymbol{k}_1,\tau_1)\, G(\boldsymbol{k}_2,\tau_1)\, G(\boldsymbol{k}_3,\tau_1), \\ {}^3T_{123} &= \int_{-\infty}^{0} \mathrm{d}\tau_{23}\, G(\boldsymbol{k}_2,\tau_{23})\, G(\boldsymbol{k}_4,\tau_{23})\, G(\boldsymbol{k}_5,\tau_{23}) \end{aligned}\right\} \tag{3.9a}$$

are the triad interaction times, defined by (3.7). We introduce the quadric interaction time

$$T_{ijkl} = \int_{-\infty}^{0} \mathrm{d}\tau\, G(\boldsymbol{k}_i,\tau)\, G(\boldsymbol{k}_j,\tau)\, G(\boldsymbol{k}_k,\tau)\, G(\boldsymbol{k}_l,\tau) = 1/[\gamma_i+\gamma_j+\gamma_k+\gamma_l]. \tag{3.9b}$$

In our case, ${}^4T_{2346}$ originates from the τ_{31} integration over the earlier time border of the intermediate time interval (filled with green in figure 7*d*) with four Green's functions

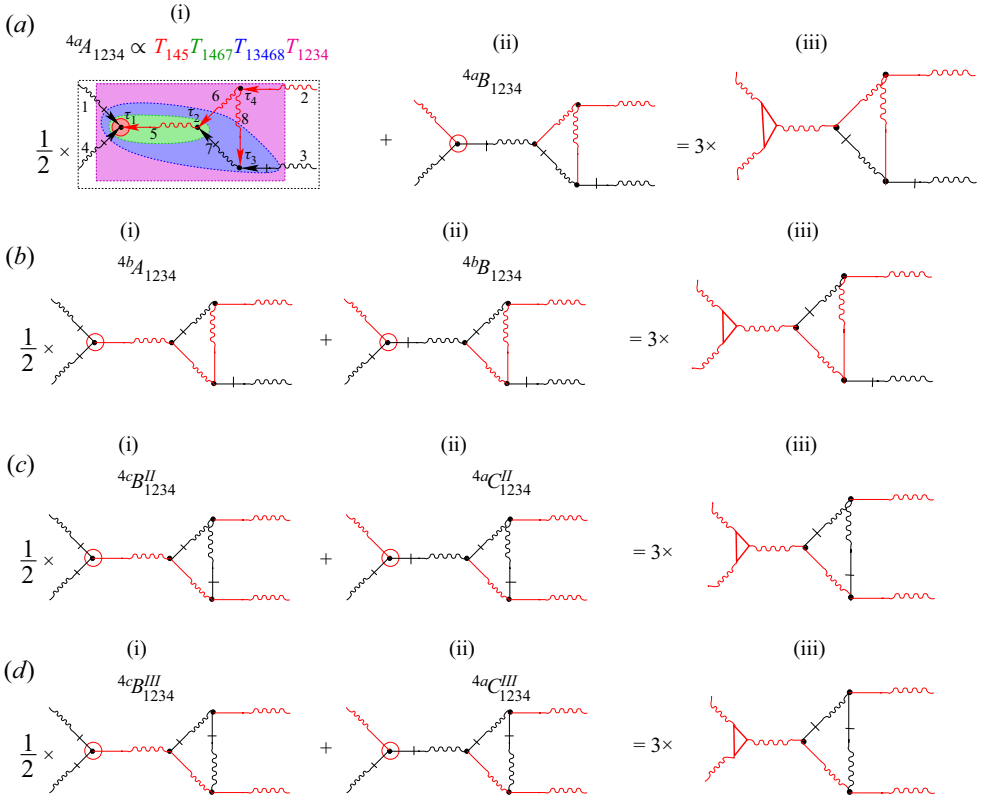

Figure 9. Second group of the triangular diagrams with earliest (145) time zone, denoted as a red circle. Notation and colour codes of the time zones and interaction times are the same as in figures 7 and 8.

directed inside of it. The oldest time interval with three incoming Green's function $G(\boldsymbol{k}_2)$, $G(\boldsymbol{k}_4)$ and $G(\boldsymbol{k}_5)$ produces $^3T_{245}$, while the earliest time interval gives T_{123} with wave vectors of the external legs. Clearly, time integrals depend only on the diagram topology and are independent of the particular type of the Green's function: true or auxiliary. Therefore, time integrals are the same for the diagram in figure 7(*b*) and many others in figure 7. Corresponding full analytical expressions for these diagrams can be found in Appendix B – see (B1), (B2) and (B3).

3.2.3. *Second-order diagrams for* $^4F^{II}_{123}$

We now consider diagrams for $^4F^{II}_{1234}$ shown in figures 10(*b*,*c*). There are two vertices with times τ_1, belonging to the earliest red-filled time zone, and $\tau_2 < \tau_1$ in the green zone. Time integration over the three Green's functions G_2, G_3 and G_5 entering the red zone leads to a factor T_{235}, while four Green's functions G_1, G_2, G_3 and G_4 entering the green zone produce T_{1234}.

Diagrams for the fourth-order contributions to $^4F^{IV}_{1234}$ are more complicated. They include four vertices and require four integrations over τ_1, τ_2, τ_3 and τ_4 with, generally speaking, more complicated topology of the time zones, not necessarily chronologically nested. Therefore, before presenting analytical expressions for their interaction times, we present in the next subsection the diagrammatic rules on how to

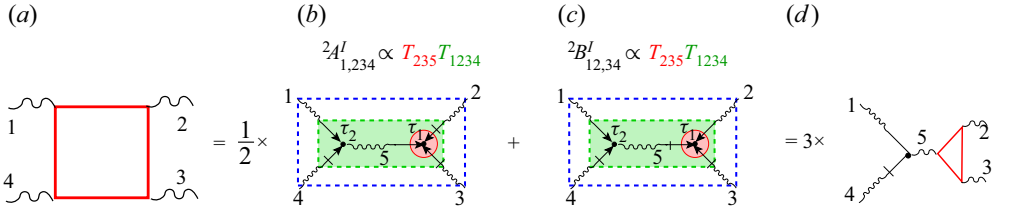

Figure 10. Diagrams for the quadruple correlator $^4\mathcal{F}^{II}_{1234}$, denoted as a thin red square in (*a*) and expressed via 'child' diagrams in (*b*) and (*c*), contributing to the simultaneous correlators. As in figures 6 and 7, interaction times T are the same in (*b*) and (*c*). Diagrams in (*b*) and (*c*) can be summarized in the diagram in (*d*), which involves triple correlator $^3\mathcal{F}^I_{235}$, shown as a thin red triangle.

reconstruct these expressions from the topology of the diagrams without their explicit calculations.

3.3. *Diagrammatic rules for the reconstruction of interaction times from the topology of the time zones*

Finding appropriate time zones that allow factorizing time integrals for the interaction times in diagrams for $^3F_{123}$ and $^4F^{II}_{123}$ described above together with more complicated situations in numerous diagrams for $^4F^{II}_{123}$, we came up with a set of rules for how to avoid explicit integrations over τ_1, τ_2, τ_3 and τ_4 in diagrams for $^4F^{IV}_{1234}$. Diagrams for $^4F_{1234}$ of any order, as well as the diagrams for higher-order correlation functions, can be divided into two major groups: weakly connected diagrams like those shown in figures 10 and 11, and compact diagrams in figures 12–14. Unlike compact diagrams, weakly connected diagrams can be divided into two parts by cutting just one line. We will show below how one can find all-time integrals in presented here two groups of four order diagrams as well as in the higher-order diagrams, by simple analysis of their topological structure. We propose the following phenomenological rules for such calculations.

(i) Partition the diagram to telescopically nested time zones as dictated by the Green's functions.

Each time zone has its 'own' vertex inside it characterized by the vertex time τ_j. Therefore the number of time zones is equal to the number of interactive vertices. Resulting time integrals will be a product of distinct time factors corresponding to each zone. Each time factor is an interaction time of the wavenumbers of Green's functions entering the zone.

(ii) In most cases, as in some diagrams in figures 8–13, times of the vertices are uniquely ordered: $\tau_1 < \tau_2 < \tau_3 < \tau_4 < 0$. In these cases, time zones are uniquely chronologically nested, having the earliest (red filled in our diagrams) time zone with τ_1, early (green) zone with $\tau_2 > \tau_1$, and recent (blue) zone with τ_3, and finally the very recent (magenta) zone with τ_4. According to rule (i), integration over these times gives the product of four interaction times; in the particular case of figure 9(*a*-i), this is $T_{145}T_{1467}T_{13468}T_{1234}$. Here, for concreteness, we coloured the interaction time according to the colour of the corresponding time zone.

(iii) In all the cases considered above and in general, the earliest (red) zone always has three incoming Green's functions, producing triple interaction time, e.g. T_{145}, in figure 9(*a*-i). The very recent zone in the triple correlator $^3F_{123}$ produces T_{123}, and in the quadruple correlator $^4F_{1234}$ produces T_{1234}. Therefore, the most recent

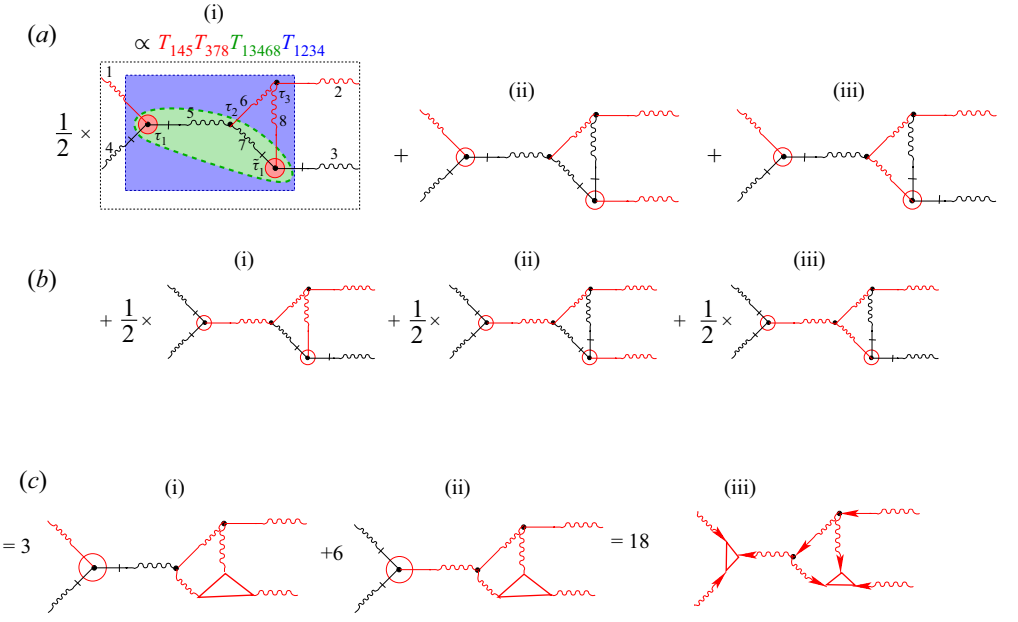

Figure 11. Third group of the diagrams with two earliest time zones. Notation and colour codes of the time zones and interaction times are the same as in previous figures. The new element here is that there are two earliest time zones, plotted as red circles. Consequently, there are two red zones, one (intermediate) green zone, and a later blue zone. The times of the earliest zones are τ_1 and $\tilde{\tau}_1$. The relationship between τ_1 and $\tilde{\tau}_1$ is not fixed, and we have two independent integrations over τ_1 and $\tilde{\tau}_1$, producing the product $T_{145}T_{378}$.

interaction time is of the same order as the correlator generating it with the same wave vector arguments. This statement is true for any-order correlations.

(iv) It may happen that a number of time zones have a relationship between times that is not determined uniquely by the Green's functions. Then there are two possibilities.

(a) Some diagrams may have two or more earliest time zones, such as those in figures 11(*a*-i) and 14(*a*-i) with two earliest time zones with τ_1 and $\tilde{\tau}_1$. In these cases, the time integral over all vertex times factorizes with the product of integrals over τ_1 and over $\tilde{\tau}_1$ from minus infinity to zero, producing the product of two (or as many as the number of earliest time zones) triple interaction times.

(b) If Green's functions do not define uniquely the ordering of times corresponding to the vertices, then the time zones are to be drawn separately for each possible ordering of interaction times. For such a case, the resulting analytical expression contains the sum of corresponding interaction times; see e.g. diagrams in figures 12(*b*-i) and 14(*a*-i). Note that such branching of regions of integrations may happen at any level except the earliest and the most recent time zones.

To summarize, the time integral for the diagram with n vertices equals the product of n interaction times, corresponding to all uniquely defined time zones Green's functions entering them. If some zones are only partially overlapping, then the frequency integral includes the sum of their interaction times.

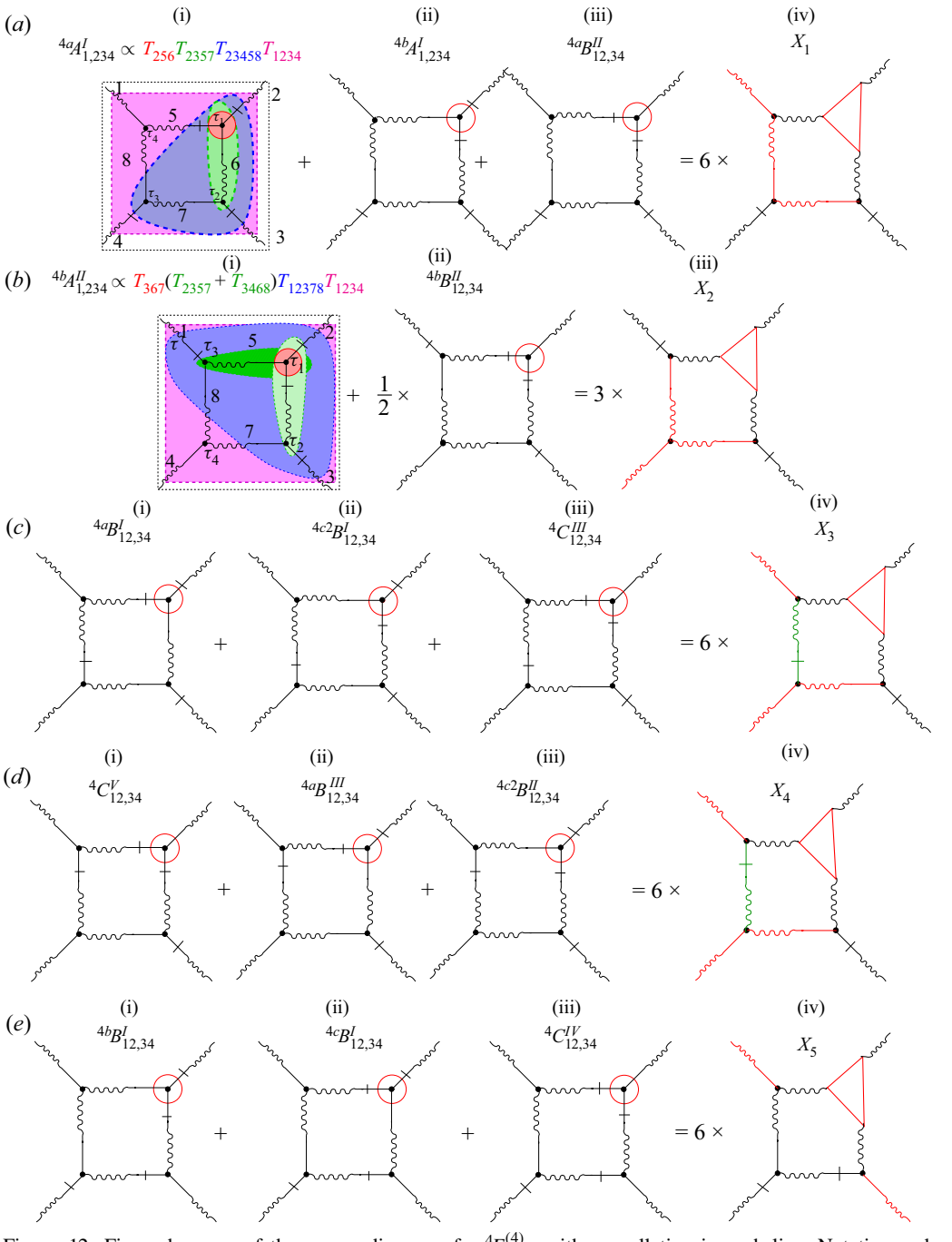

Figure 12. Five subgroups of the square diagrams for $^{4}F^{(4)}_{1234}$ with cancellation in each line. Notation and colour codes of the time zones and interaction times are the same as in previous figures. The new element appears in (*b*-i): the relationship between τ_2 and τ_3 is not dictated by the orientation of the Green's functions. Consequently, integrations over τ_2 and τ_3 are performed differently in these two cases. If $\tau_2 < \tau_3$, then the τ_2 integration occurs over the region coloured in light green, while the $\tau_2 > \tau_3$ region is coloured in darker green. Such a partition of integration regions leads to the sum of two contributions $(T_{2357} + T_{3468})$ originated from these two green zones.

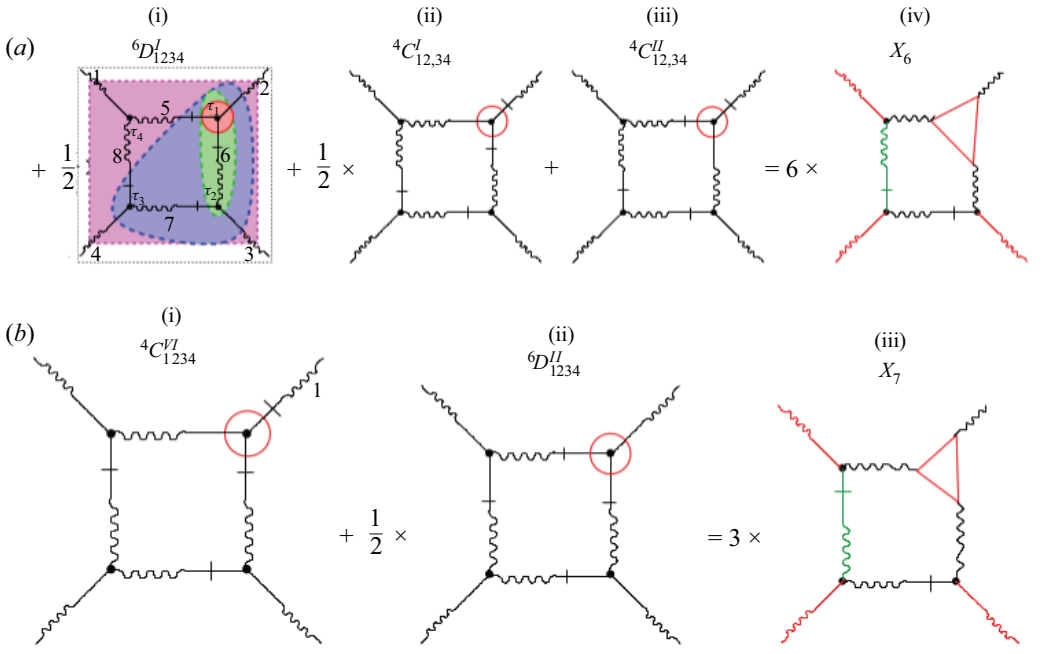

Figure 13. The next two subgroups of the square diagrams for $^4F^{(4)}_{1234}$, which sum to the triple correlator shown on the right of each row as a red triangle.

4. Triangular re-summation of the triple-line reducible triads

4.1. *Triangular re-summation of diagrams for triple correlators* $^3F_{123}$

In this subsection, we will bring all the things we have considered together and introduce triangular re-summation of the triple correlator, the latter being the main focus of this work. It has three appearances, shown in figure 1: empty thin red triangle for first-order contribution $^3F^I$, empty thick red triangle for third-order contribution $^3F^{III}$, and filled thick red triangle for the full correlator ^3F.

One of the main points of this paper may be recognized by comparing diagrams for $^3F^I$ in figure 6 and for $^3F^{III}$ in figure 7. Note that our definition of the correlator involves the permutation operator $\boldsymbol{P}_{123}$, defined by (2.12*a*) and (2.13). First notice that (*d*–*i*) of figure 7 contain a vertex marked by a red circle, and the Green's functions connected to this vertex form precisely the diagrams of the $^3F^I$ shown in figure 6. As we will see below (see (4.6)), this fact allows us to write a compact expression for $^3F^{III}$,

$$\left.\begin{aligned} {}^3F^{III}_{123} = \boldsymbol{P}\int \frac{\mathrm{d}\boldsymbol{k}_4}{(2\pi)^d}\, {}^4T_{2346}V_{146}\times[V_{425}F_2 + V_{245}F_4]\,{}^3F^I_{356}, \\ \boldsymbol{k}_5 = \boldsymbol{k}_4+\boldsymbol{k}_2 \text{ and } \boldsymbol{k}_6 = \boldsymbol{k}_4-\boldsymbol{k}_1, \end{aligned}\right\} \tag{4.1}$$

expressed in terms of the first-order correlator as follows from figures 7(*g*,*h*). This fact has deep consequences, as we will see below.

The permutation operator $\boldsymbol{P}_{123}$ acting on the two diagrams of figure 7 produces six diagrams. These diagrams can be grouped into a triad of diagrams that involves three vertices, with rotational C_3 symmetry, and three tails of Green's functions ordered chronologically inside the triangle from the present time $t = 0$ in the simultaneous

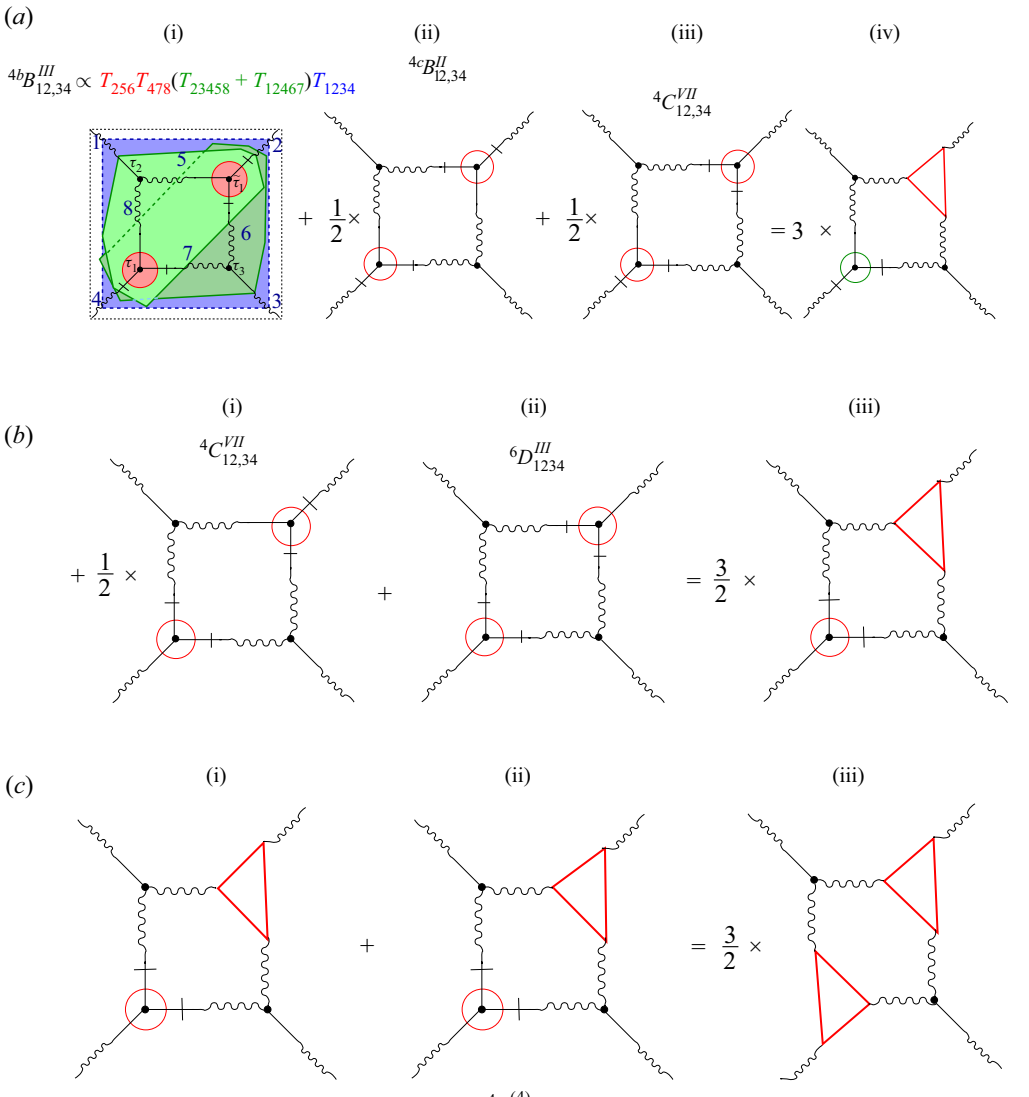

Figure 14. The last group of the square diagrams for $^{4}F^{(4)}_{1234}$, with two earliest time zones producing the product $T_{256}T_{478}$. As in figure 12(*b*-i), the relationship between τ_2 and τ_3 resulting in the sum of two contributions $(T_{23458}+T_{12467})$ originated from two overlapping green zones.

correlator back to all past times $t_j < 0$, as required by the casualty principle. We will refer to this object as a 'third-order triad' and depict it by the thick red triangle.

Notice that the bare Green's function and bare double correlation in the Dyson–Wyld line re-summation are called reducible fragments, which can be separated from the body of a diagram by cutting two lines. Bearing this in mind, we can clarify them as 'double-line' reducible diagrams. Such a name immediately suggests the existence of 'triple-line reducible diagrams'. Indeed, our triad diagrams can be separated from the body of a diagram by cutting three Green's functions entering this time zone. We call these objects 'triple-line reducible triads' (of C_3 symmetrical groups of diagrams). Up to now, we met in figure 6 first-order triple-line reducible triads (with one vertex) and in figure 7 third-order triple-line reducible triads with three vertices, shown e.g. in figure 7(*d*) by a blue square.

Let us examine again figure 7(*d*). The red (oldest) time zone has three incoming Green's functions entering it with straight lines. The red time zone is in turn inside the earlier, blue time zone, which has three straight lines entering it. This is an example of the triangular telescopically nested time-ordered reducible triads. Higher-order diagrams for the simultaneous triple correlators will have multiple zones nested in similar manner. These zones will sum up the fully dressed triple correlator.

Indeed, analysis of the higher-order diagram for ${}^3F$ shows that besides two first-order triads in the first row of figure 7 (thin red triangles) one finds diagrams in which instead of the first-order triads, one meets third-order triads (thick red triangles). These diagrams represent fifth-order triads, which in turn can be found in even higher-order diagrams, etc. This possibility originates first from the fact that the perturbation diagrammatic series involves all topologically possible diagrams, and second because all diagrammatic rules, including $1/N$ symmetry rules and time integration rules, are applicable not only to the whole diagrams but also to any of their fragments. Therefore, there is a mechanism for the infinite resuming of telescopically nested, chronologically ordered triple-line reducible triads, appearing instead of the earliest time zones, resulting in the fully dressed triple correlator ${}^3F_{123}$.

The Dyson line re-summation leads to a fully dressed Green's function. The Wyld re-summation leads to the fully dressed double correlator. The triangular re-summation of the triple-line reducible triads suggested here leads to a fully dressed simultaneous triple correlator, as we will show in § 4.3.

4.2. *Triangular re-summation of diagrams for quadruple correlators* ${}^4F_{1234}$

4.2.1. *Identifying* ${}^3F^I$ *triad in diagrams for* ${}^4F^{II}$

Analysing the second-order diagrams ${}^2\mathcal{A}_{1,234}$ and ${}^2\mathcal{B}_{12,34}$ for ${}^4\mathcal{F}_{1234}$, shown in figures 3(*b*,*c*), as before, we replace the (three) double correlators by a sum of two auxiliary Green's functions according to (3.2). In such a case, each of the diagrams produces 2^3 diagrams. Out of those $2\times 2^3 = 16$ diagrams, only three of them, shown in figures 10(*a*,*b*), survive for the same-time case after frequency integration required by (3.1*b*). Note that the diagram in figure 10(*b*) appears twice in different orientations. This removes the factor $1/2$ in front of it. The disappearance of the $1/2$ factor occurs as a manifestation of the $1/N$ symmetry rule because the diagram in figure 10(*b*) lost reflecting symmetry with respect to the vertical line, present (together with prefactor $1/2$) in the diagram depicted in figure 3(*c*).

Analytically, diagrams in figure 10 can be written as ${}^4F^{II}_{1234} = \underset{1234}{\boldsymbol{P}}[{}^2A_{1,234} + {}^2B_{12,34}]$, where

$$ {}^2A_{1,234} = \tfrac{1}{2}V_{14\bar5}V_{523}F_2F_3F_4T,\ {}^2B_{12,34} = F_3F_4F_{1+4}V_{13\bar5}V_{235}T,\ \ T \equiv T_{1234}T_{235}, \quad (4.2a) $$

with $\boldsymbol{q}_5 = \boldsymbol{q}_1 + \boldsymbol{q}_4 = -(\boldsymbol{q}_2 + \boldsymbol{q}_3)$. The time integral T here was found with the help of diagrammatic rules formulated in § 3.3. It reduces to a product of the triad and quartic interaction times. Together with diagrams in figures 6(*e*–*g*), this allows us to recognize that the sum of the diagrams presented in figures 10(*b*,*c*) include the correlator ${}^3F^I_{235}$, shown in figure 10(*d*) as red filled circle. Analytically, this reads

$$ {}^4F^{II}_{1234} = 3T_{1234}(V_{145}F_4)F^I_{235}. \quad (4.2b) $$

We see that the first contribution of ${}^4F^{II}_{1234}$ to the four-point correlator contains the first contribution ${}^3F^{I}_{235}$ to the three-point correlator. We will show below that this statement generalizes to higher orders as follows. The $(n+1)$th order of ${}^4F^{n+1}_{1234}$ involve an nth-order contribution of ${}^3F^{n}$. Consequently, the fully dressed fourth-order correlator depends on the fully dressed third-order correlator. This is the essence of the triangular re-summation, and it underlines the key role played by the third-order correlator.

4.2.2. *Identifying ${}^3F^{I}$ and ${}^3F^{III}$ triads in the weakly connected spine diagrams for ${}^4F^{IV}$*
Recall that diagrams in figures 10(*b*,*c*) are weakly connected in the sense that they can be divided into two parts by cutting only one line, sometimes referred to as a 'spine'. Using diagrammatic rules for ${}^4F^{(4)}_{1234}$ formulated in § 2.4, we found all the weakly connected spine diagrams shown in figures 8, 9 and 11. We divide the diagrams into these three figures by the position of the earliest (red) time zone relative to the spine G_5. Figure 8 shows 18 diagrams with the earliest time zone to the right of the Green's function G_5 in the (678)-triangle; figure 9 includes 8 diagrams with the (145)-time zone to the left of G_5; and figure 11 involves six diagrams with two earliest times on either side of G_5.

The diagrams of figures 8, 9 and 11 are grouped in such a way that the triple correlator ${}^3F^{I}$ is identifiable in each row. That is, each line contains equivalent diagrams except for the position of the true Green's function entering the earliest time zone. Consequently, each row sums to the diagram in the right-hand column containing the third-order correlator in the third-order ${}^3F^{III}$ shown as a thin red triangle.

Consider the diagrams in figure 8. The six resulting diagrams on the right-hand side have the same structure connecting two parts by leg 5. One part is the block of $G_1G_4V_{145}$ with three legs. The second part consist of the structures in which we recognize one of the diagrams for ${}^3F^{III}$, shown figure 7.

Therefore, similarly to (4.2*b*), the sum of all diagrams in figure 8 for ${}^4F^{IV}$ (denoted as ${}^{4,\alpha}F^{IV}_{1234}$) can be presented via ${}^3F^{III}$:

$$ {}^{4,\alpha}F^{IV}_{1234} = 3\,T_{1234}(V_{145}F_4)\,{}^3F^{III}_{235}. \tag{4.3a} $$

Comparing (4.2*b*) and (4.3*a*), we see that: (i) the fourth-order correlator ${}^4F^{n+1}_{1234}$ of any order always includes quadruple interaction time T_{1234}, originated from integration in the latest time zone with four external legs of the Green's function $G_1G_2G_3G_4$; (ii) the earliest time zone, (235) in this case, denotes the place where the triple correlator appears after the triangular re-summation.

Considering diagrams with the earliest (145) time zone in figure 9, we see that figures 9(*a*–*d*) have the same structure, summed to the triple correlator ${}^3F^{I}_{145}$ times three-point objects, denoted as X^A, X^B, X^C and X^D. The sum of these diagrams is given by

$$ \left.\begin{aligned} {}^{4,\beta}F^{IV}_{1234} &= 3T_{1234}\,{}^3F^{I}_{145}[X^A_{5,23}+X^B_{5,23}+X^C_{5,23}+X^D_{5,23}], \quad \boldsymbol{k}_5=\boldsymbol{k}_1+\boldsymbol{k}_4,\\ X^A_{5,23} &= V_{567}V_{6\bar{2}8}V_{8\bar{3}7}F_3F_4, \quad X^B_{5,23}=V_{756}V_{268}V_{8\bar{3}7}F_3F_6, \quad \ldots. \end{aligned}\right\} \tag{4.3b} $$

Equations for $X^C_{5,23}$ and $X^D_{5,23}$ in (4.3*b*) can be reconstructed easily from their diagrammatic representation in figure 9.

The last group of the weakly connected spine diagrams with two earliest time zones is shown in figure 11. These diagrams sum up into one diagram, with the product of two

triple correlators shown in in figure 11(*c*-iii). The corresponding analytical expression is

$$^{4,\gamma}F^{IV}_{1234} = 9T_{1234}\,{}^{3}F^{I}_{145}\int \frac{\mathrm{d}\boldsymbol{k}_6}{(2\pi)^d}\,T_{13468}\,{}^{3}F^{I}_{378}V_{268}V_{657}. \tag{4.3c}$$

Remarkably, this contribution is proportional to the square of the triple correlator $^{3}F^{I}$.

4.2.3. *Identifying $^{3}F^{I}$ in the compact square diagrams for $^{4}F^{IV}$*

As seen in figure 5, there are eight compact 'square' diagrams for the quadruple correlator $^{4}F^{IV}$. Consequently, they produce $8\times 2^4 = 128$ child diagrams, but only 22 of them, shown in figures 17 and 18, contribute to the simultaneous correlator. Similar to the previous subsubsection, here we show how all of them can be grouped in triads, each of which represents the triple correlator $^{3}F^{I}$. We identify the triads of diagrams such that all elements in the diagrams in each triad are identical, except one vertex, where the 'true' Green's function occupies each of the three positions in turns, and the other two positions are occupied by auxiliary Green's functions.

First, we separate all diagrams into two groups: those with one earliest time zone shown in figures 12 and 13, and those with two earliest time zones shown in figure 14.

The biggest group with one such zone will be further divided into several topologically different subgroups as follows. Since the diagrams are under the permutation operator, we redraw the diagrams (by rotations or by mirroring) in such a way that the earliest time zone will be placed in the upper right corner of the diagram marked by red circle. We then label all lines as shown e.g. in figure 12(*a*-i).

Now we will classify the diagrams by the number of the external real Green's functions on the vertex 1, 3 and 4. We call the diagrams 'identical by Green's functions' if their external Green's functions are identical. This set of lines does not include lines labelled by 2, 5, which connect to the earliest time zone. We recall that all vertices must be connected to one of the external true Green's functions by the true Green's functions with the same orientations.

In a subgroup with at least one true Green's-function there are two options: in which either G_1 or G_2 are true Green's function. The subgroup in which G_3 is a true Green's function is not distinct: it topologically coincides with the G_1 subgroup by mirroring in the 2–4 line that connects G_2 and G_4.

Consider the subgroup of diagrams with external true Green's function G_1. These diagrams are shown in figure 12 (*a*-i *a*-iii). From general requirements, its topology must include G_7 and G_8 true Green's functions that connect 3- and 4-vertices to a 1-vertex with true Green's function G_1. This subgroup has only three diagrams, shown in figures 12(*a*-i), 12(*a*-ii) and 12(*a*-iii). These three diagrams form the first triad, which sums to the diagram in figure 12(*a*-iv) that involves the triple correlator $^{3}F^{(1)}_{256}$.

Next, the G_4 subgroup must include G_7 and G_8 true Green's functions that connect the 4 vertex with 3- and 1-vertices. This subgroup has only two diagrams, shown in figures 12(*b*-i) and 12(*b*-ii), forming the triad that sums to the diagram in figure 12(*b*-iii) that involves the triple correlator.

There are nine diagrams with two true Green's functions labelled either 1 and/or 3 and 4. The first six diagrams involve G_1 and G_4. Three of them, collected in figures 12(*c*-i), 12(*c*-ii) and 12(*c*-iii), have auxiliary Green's function G_8, oriented down by a straight line. They are summarized in the diagram in figure 12(*c*-iv) that involves the same triple correlator $^{3}F^{(1)}_{256}$. The remaining three diagrams with auxiliary Green's functions G_8,

oriented up, are summarized in the diagram in figure 12(*d*-iv). The last triad with two real Green's functions G_1 and G_3 create the diagram in figure 12(*e*-iv), with the same triple correlator ${}^3F^{(1)}_{256}$.

The subgroup with three true Green's-functions G_1, G_2 and G_3 is shown in figure 13. They create two subgroups, with auxiliary Green's function G_8 oriented either up or down. The first triad creates a diagram in figure 13(*a*-iv). Considering the diagram in figure 13(*b*-i) as two diagrams (with prefactor 1/2) and rotating one of them around the 2–4 line, we have a second triad that creates the diagram in figure 13(*b*-iii).

Analytical expressions for ${}^{4\delta}F^{IV}_{1234}$, originated from diagrams $X_1, X_2, \ldots, X_7$ depicted in figures 12 and 13, are as follows:

$$\left.\begin{gathered}
{}^{4\delta}F^{IV}_{1234} = T_{1234}\,\underset{1234}{\boldsymbol{P}}\left\{\int \frac{\mathrm{d}\boldsymbol{k}_5}{(2\pi)^d}\,{}^3F^{(1)}_{256}J^{\square}_{1234}\right\},\\
\boldsymbol{k}_6 = \boldsymbol{k}_2 + \boldsymbol{k}_5, \quad J^{\square}_{1234} = \sum_{i=1}^{7} X_i,\\
X_1 = 6T_{2357}T_{23458}V_{1\bar{5}8}V_{\bar{7}36}V_{\bar{8}47}F_3F_4,\\
X_2 = 3(T_{2357}+T_{1268})T_{12378}V_{81\bar{5}}V_{\bar{7}63}V_{47\bar{8}}F_1F_3,\\
X_3 = 6T_{2357}T_{23458}V_{1\bar{5}8}V_{\bar{7}36}V_{47\bar{8}}F_3F_8, \quad X_4 = 6T_{2357}T_{23458}V_{1\bar{5}8}V_{\bar{7}36}V_{47\bar{8}}F_3F_8,\\
X_5 = 6T_{2357}T_{23458}V_{1\bar{5}8}V_{\bar{7}36}V_{\bar{8}47}F_4F_7, \quad X_6 = 6T_{2357}T_{23458}V_{1\bar{5}8}V_{36\bar{7}}V_{47\bar{8}}F_7F_8,\\
X_7 = 6T_{2357}T_{23458}V_{1\bar{5}8}V_{36\bar{7}}V_{47\bar{8}}F_7F_8.
\end{gathered}\right\} \tag{4.4}$$

The 'square' superscript denotes the sum of the square diagrams in figures 12 and 13. The second group of diagrams with two earlier time zones consists only of four diagrams. We used the diagram ${}^4C^{VII}$ in figures 14(*a*-iii) and 14(*b*-i), putting prefactor 1/2 in front of them. After that, figures 14(*a*-i), 14(*a*-ii) and 14(*a*-iii) are summed to figure 14(*a*-iv), and figures 14(*b*-i) and 14(*b*-ii) are summed to figure 14(*b*-iii). In turn, figures 14(*a*-iv) and 14(*b*-iii) (repeated as figures 14(*c*-i) and 14(*c*-ii)) can be summed to figure 14(*c*-iii), which involves two triple correlators, ${}^3F^{I}_{256}$ and ${}^3F^{I}_{478}$. An analytical expression for the sum of all diagrams with two earliest time zones is

$${}^{4\varepsilon}F^{IV}_{1234} = T_{1234}\,\underset{1234}{\boldsymbol{P}}\left\{\int \frac{\mathrm{d}\boldsymbol{k}_5}{(2\pi)^d}\,{}^3F^{I}_{256}\,{}^3F^{I}_{478}\times(T_{23458}+T_{12467})V_{15\bar{8}}V_{3\bar{6}7}\right\}. \tag{4.5}$$

Similar to (4.3*c*), here the contribution to the fourth-order four-point correlator comes from the product of two three-point correlators of the first order, ${}^3F^{I}_{123}$. Analysing the structure of the diagrammatic technique, we expect that in the higher-order diagrams, terms with a product of three or more correlators ${}^3F^{I}_{123}$ will appear.

4.3. *Full triangular re-summations for* ${}^3F_{123}$ *and* ${}^4F_{1234}$

In the previous subsections, we demonstrated how the sum of six initial diagrams for ${}^3F^{III}_{123}$ presented in figure 7 fuses into two diagrams in figures 7(*b*,*c*) involving ${}^3F^{I}$. Similarly, the sum of two diagrams for ${}^4F^{II}_{1234}$ in figure 10 combines to one diagram figure 10(*d*) with ${}^3F^{I}$. Moreover, the sum of 18 diagrams for ${}^4F^{IV}_{1234}$ in figure 8 combines to six diagrams involving ${}^3F^{I}$, which in turn fuse into just one diagram with ${}^3F^{III}$, presented analytically by (4.3*a*).

In exactly the same way, the rest of the diagrams for ${}^4F^{IV}_{1234}$ shown in figures 9–14 were summarized in these figures to diagrams involving the triple correlator ${}^3F^{I}$. These findings are not a miracle, but a deep consequence of fundamental features of the perturbation approach reflected in the diagrammatic technique and the crucial role that is played by the three-point correlator.

Namely, the diagrammatic series involves all topologically possible diagrams, satisfying general restrictions, described in § 2.4. These restrictions together with the $1/N$ rule, prescribing the numerical prefactor, have local character, i.e. they are applicable to the entire diagram, or to any of its fragments. For example, any diagram for ${}^3F_{123}$ has three external Green's functions G_1, G_2 and G_3 entering the diagram by straight lines. Similarly, any earliest time zone also has three 'boundary' Green's functions, say G_k, G_l and G_m, entering the zone in the same way. Therefore, the sum of all diagrams inside the earliest time zone of $(2n+1)$th order (with $(2n+1)$ vertices) gives exactly the triple correlator of $(2n+1)$th order, ${}^3F^{n+1}_{klm}$. This is exactly what happened in all diagrams with the first-order earliest time zones (coloured in red), summarized to ${}^3F^{I}$, while the diagrams in figure 8 with the third-order earliest time zones (coloured in blue) were summarized to ${}^3F^{III}$.

Consider first full triangular re-summation for the triple correlator ${}^3F_{123}$. Figure 15(*a*) just resembles the diagram in figure 6(*b*) for ${}^3F^{I}_{123}$, while figure 15(*b*-i–*b*-iii) shows re-summation diagrams for ${}^3F^{III}_{123}$, with the result ${}^3F^{III}_{123} \propto {}^3F^{I}_{123}$, as indicated by (4.1). The next step is shown in figure 15(*b*). Comparing figures 15(*b*) and 15(*c*), we see the pattern that illustrates the essence of the triangular re-summation. Namely, ${}^3F^{III}_{123}$ depends on ${}^1F^{I}_{123}$ in the same way as ${}^3F^{V}_{123}$ depends on ${}^3F^{III}_{123}$. We can continue this iteration *ad infinitum*; see the result in figure 15(*c*). Clearly, this procedure does not create high-order diagrams for ${}^3F^{III}_{123}$ of a more complicated topological structure. These diagrams are replaced by '…' (an ellipsis) in figure 15(*c*), which presents the entire series for ${}^3F = {}^3F^{I}_{123} + {}^3F^{III}_{123} + {}^{3!}F^{V}_{123} + \cdots$. Analytically, we have

$$ {}^3F_{123} = {}^3F^{I}_{123} + 6 \underset{123}{\boldsymbol{P}} \int \frac{\mathrm{d}\boldsymbol{k}_4}{(2\pi)^d}\, T_{2346} V_{146} \times [V_{425} F_2 + V_{245} F_4]\, {}^3F_{356} + \cdots . \tag{4.6} $$

This equation represents the essence of triangular re-summation for the fully dressed triple correlator ${}^3F_{123}$, as it represents ${}^3F_{123}$ through the infinite series that itself involves ${}^3F_{123}$. If one neglects higher-order contributions replaced in (4.6) by an ellipsis, then this equation becomes a closed equation for ${}^3F_{123}$. Clearly, this procedure is an uncontrolled approximation. Currently, this equation looks linear since the higher-order terms are represented as an ellipsis. Analysing higher-order contributions, we found diagrams with two, three and more earliest time zones, giving birth to contributions to (4.6) proportional to $({}^3F)^2$, $({}^3F)^3$, and so on.

Based on (4.6), consider an inverse energy cascade in the fractional dimension $d = \frac{4}{3} + x$ close to the critical dimension $d_0 = \frac{4}{3}$. Here, there are two limiting cases: (i) constant energy flux ε, or (ii) constant energy ${}^2F$. When $\varepsilon = \text{const}$ in the limit $x \to 0$, the energy is ${}^2F \to \infty$. We focus on the latter case, when the energy ${}^2F(\boldsymbol{k})$ is kept finite. Then in the limit $x \to 0$, the energy flux ε (together with ${}^3F$) vanishes. In this case, (4.6) becomes a nonlinear homogeneous equation with powers of full triple correlators on its right-hand side. This equation has a trivial solution ${}^3F_{123} = 0$. This is a demonstration that the triple simultaneous correlator is zero under these assumptions ($d = \frac{4}{3}$ and finiteness of

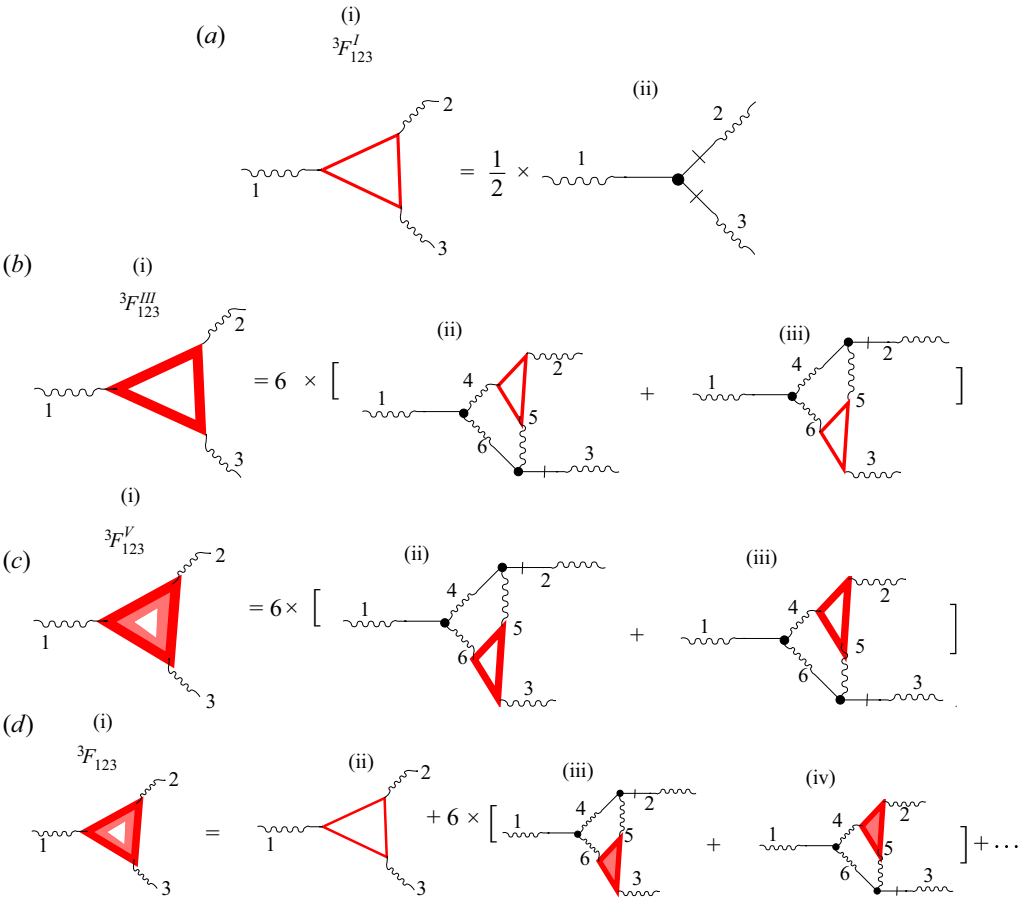

Figure 15. First triple-irreducible diagrams in the triangular re-summation for $^3F^{(\infty)}$: (*a*) the $^3F^I_{123}$ correlator; (*b*) the $^3F^{III}_{123}$ correlator; and (*c*) the $^3F^V_{123}$ correlator. (*d*) Diagrams yielding integral equation (4.6) as a result of full triangular re-summation for $^3F_{123}$. Triangular re-summation of the full triple correlator given by (4.6): the full triple correlator (filled triangle) is expressed as a sum of a bare triple correlator (thin triangle) and an infinite diagrammatic series that depends on the triple correlator itself.

the energy), not only in the leading order (as shown in L'vov *et al.* 2002) but in all orders, i.e. fully dressed correlator $^3F = 0$.

The diagrams for the four-point simultaneous correlator $^{4!}F_{1234}$ can also be triangular re-summed. This is shown in figure 16. We denote $^4F_{1234}$ as a red thick-filled square. The simplest diagram, in figure 16(*a*-ii), originates from the infinite re-summation of the diagram for $^4F^{II}_{1234}$ in figure 10(*d*), where $^3F^I$ is summed up to the full correlator. Graphically, this part of the triangular re-summation is depicted by replacing the thin triangle by thick filled triangle. The triangular re-summation includes all diagrams in figure 8. Four rows of diagrams in figure 9 (after inversion over a spine Green's function G_5) serve as the first terms of the triangular re-summation that leads to diagrams in figures 16(*a*-iii)–16(*a*-vi). In the same way, diagrams in figure 11 produce figure 16(*a*-vii), proportional to $(^3F)^2$, and compact square diagrams in figures 12 and 13 give, after re-summation, diagrams in figures 16(*b*-i) and 16(*b*-ii). Remarkably, compact square

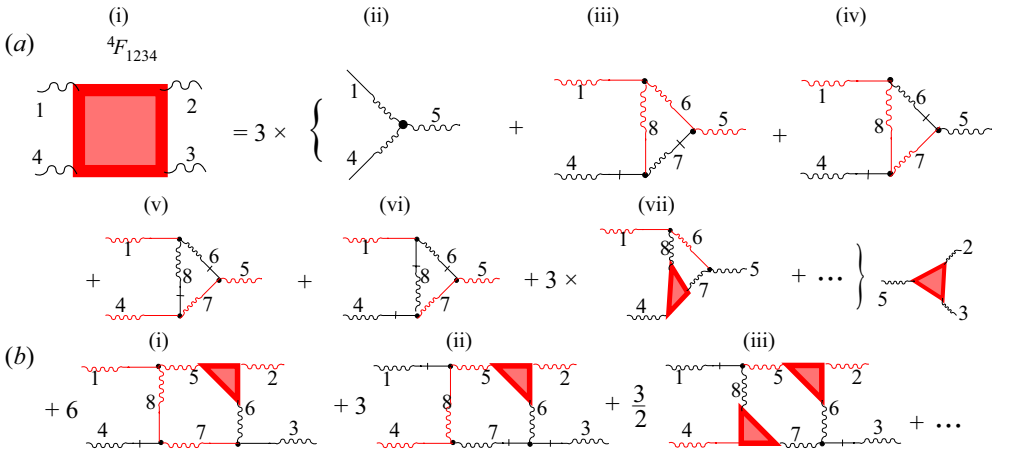

Figure 16. Full triangular re-summation for the four-point correlator ${}^4F_{1234}$.

diagrams in figure 14 with two earliest time zones create the diagram in figure 16(*b*-iii). This diagram is proportional to the square of the full triple correlator ${}^3F$. Higher-order terms, represented by dots, can also be triangular re-summed.

Analytical expressions for various contributions to ${}^4F_{1234}$, denoted ${}^4F^{A1}_{1234}, \ldots, {}^4F^{A6}_{1234}$, ${}^4F^{B1}_{1234}$, ${}^4F^{B2}_{1234}$ and ${}^4F^{B3}_{1234}$, can be reconstructed straightforwardly from the corresponding diagrams, e.g.

$$\left.\begin{aligned}
{}^4F^{A1}_{1234} &= 3\,{}^3F_{235}F_4V_{145},\\
{}^4F^{A2}_{1234} &= 3\,{}^3F_{235}F_4\int\frac{\mathrm{d}\boldsymbol{k}_6}{(2\pi)^2}\,V_{168}V_{657}V_{847}F_7, \quad \ldots\\
{}^4F^{A6}_{1234} &= 9\,{}^3F_{235}\int\frac{\mathrm{d}\boldsymbol{k}_6}{(2\pi)^2}\,V_{168}V_{657}\,{}^3F_{235},\\
{}^4F^{B1}_{1234} &= 6F_3F_4\int\frac{\mathrm{d}\boldsymbol{k}_5}{(2\pi)^2}\,V_{156}V_{847}V_{673}\,{}^3F_{256}, \quad \ldots\\
{}^4F^{B3}_{1234} &= \frac{3}{2}\int\frac{\mathrm{d}\boldsymbol{k}_5}{(2\pi)^2}\,V_{158}V_{367}\,{}^3F_{256}\,{}^3F_{478}.
\end{aligned}\right\} \tag{4.7}$$

These equations present fully dressed quadruple correlator ${}^4F_{1234}$ as a series in powers of fully dressed triple correlator ${}^3F$, explicitly involving linear and quadratic contributions. Some diagrams with five or more vertices will give contributions of third, fourth and higher powers of ${}^3F$.

In particular, this means that in the inverse energy cascade in a dimension near the critical $d = \frac{4}{3} + x$, the dressed fourth-order correlator ${}^4F_{1234}$ vanishes in the limit $x \to 0$ with finite energy. Moreover, there is every reason to believe that this statement is valid for all high-order correlators ${}^nF$ with $n = 4, 5, \ldots$. If so, then the statistics of turbulence in $d = \frac{4}{3}$ becomes Gaussian when all cumulants vanish, and is very close to the Gaussian statistics for $d = \frac{4}{3} + x$. We think that this explains the experimental observation that the statistics of the inverse energy cascade is close to Gaussian even for $d = 2$.

5. Summary

In this paper, we reconsider the perturbation theory for hydrodynamic turbulence via the Dyson–Wyld diagrammatic technique, presenting detailed analyses of the three-point and four-point velocity correlation functions in leading and next order. This corresponds to the first and third orders in the interaction amplitude for the triple correlator, and to the second and fourth orders for the four-point correlator. This allowed us to recognize the crucial role played by the triple correlator and the energy flux over scales, and to clarify their role in determining the entire statistics of turbulence. In the framework of the Dyson–Wyld diagrammatic technique, we performed the following steps.

(i) We showed how to build diagrammatic series for the complex amplitude of strongly interacting fields.

(ii) We showed how to build diagrammatic series for the three-point, four-point and higher-order correlation functions in the velocity. This is achieved by averaging over an ensemble of random force, or gluing together diagrams for the velocity field (trees). In doing so, we have demonstrated constructively the natural emergence of the $1/N$ symmetry rule, which prescribes the numerical prefactor of a diagram via the number N of elements of its symmetry group.

(iii) We then considered simultaneous velocity correlators. In doing so, we needed to perform the integration over all possible frequencies of multiple time correlators. To achieve this goal, it is imperative to know the frequency dependence of the double correlator and Green's function. We have assumed the one-pole approximation for the frequency dependence of double correlator and Green's function. This assumption led to the decoupling of all the double correlators into the sum of two auxiliary Green's functions pointed in different directions. This, in turn, allowed us to formulate time integration rules by introducing time zones and time boundaries. These rules allow one to reconstruct the time integrals from the topology of the diagrams without explicit calculations of the high-order time integrals.

(iv) We then considered in detail the simultaneous triple correlator of the velocity in the first and third order in the interaction vertex. We have shown how the diagrams can be grouped into triads, thus leading to the triple correlator. This grouping allowed us to formulate the triangular re-summation. The triangular re-summation does for the triple-reducible diagram what Dyson–Wyld re-summation does for double-reducible diagrams. Namely, the triangular re-summation replaces the bare triple correlator by its 'dressed' counterpart.

(v) We considered a four-point correlator in the second and fourth orders. We showed that the triangular re-summation is equally applicable to four-point simultaneous correlators. We did this by identifying a third-order simultaneous velocity correlator in the diagrammatic series for four-point correlators. We did it constructively for the second-order and fourth-order diagrams. Analysing the structure of the diagrammatic technique, we showed that this pattern continues for all correlators for any order in the perturbation theory. Namely, all the diagrams can be grouped together in triple-reducible diagrams, i.e. the groups where the diagrams are equivalent except for one vertex where the Green's function is rotated. These groups can be re-summed to become third-order simultaneous correlators.

(vi) Considering diagrammatic series of the perturbation theory for any-order correlation functions ${}^{n}F$, we demonstrated that they can be reordered (re-summed) such that ${}^{n}F$ includes explicitly one or more series for ${}^{3}F$. From a physical viewpoint, this means

that ${}^nF$ is a polynomial in powers of ${}^3F$, without a zero-order term. In particular, this means that if ${}^3F$ vanishes (as happens in thermodynamic equilibrium), then all irreducible diagrams ${}^nF$ (i.e. cumulants of the high-order correlators) vanish as well, and statistics of turbulence becomes Gaussian. Bearing in mind that the energy flux over scales $\varepsilon(\boldsymbol{k})$ is proportional to ${}^3F$, we conclude that this flux governs not only the energy distribution over scales (i.e. ${}^2F$), as Kolmogorov assumed in 1941, but the entire statistics of hydrodynamic turbulence. We stress that this conclusion is based not on any truncation of the diagrammatic series, but on their analysis as a whole.

(vii) As explained in L'vov *et al.* (2002), the turbulence inverse energy cascade coincides with the thermodynamical equilibrium for the fractional dimensions $d = \frac{4}{3}$. Therefore it is exactly Gaussian. The difference between $\frac{4}{3}$ and $d = 2$ is a small parameter $\epsilon = d - \frac{4}{3}$. The last observation explains therefore why the 2-D turbulence is close to the Gaussian state. As ${}^3F^I_{123} \propto \epsilon$, the triangular re-summation determined by (4.6) shows that the full correlator ${}^3F_{123}$ is also small. If ${}^3F_{123}$ is small, then figure 16 explains why the fourth-order cumulant is also small. In this way, in 2-D turbulence, cumulants ${}^nF$ become presented as a series in powers of the small parameter $\epsilon = d - \frac{4}{3} = \frac{2}{3}$, thus demonstrating the closeness of the 2-D statistics to the Gaussian case.

Note also that the triangular re-summation of the triads is possible only for the one-time correlators; otherwise, for example, diagrams such as those shown in figures 6(*b–d*) have to be accounted for. From a theoretical viewpoint, this is the consequence of the fact that in the thermodynamic equilibrium, the only simultaneous statistics are Gaussian (with all cumulants of the correlation functions vanishing).

We hope that this paper provides a solid theoretical foundation for the further analytical study of the statistics of highly developed 2-D and 3-D hydrodynamic turbulence, and other systems of hydrodynamic type.

Acknowledgements. We would like to express our gratitude to the anonymous referees for their valuable feedback, which significantly helped us to improve this paper.

Funding. Y.V.L. acknowledges support from the NSF DMS award 2009418.

Declaration of Interests. The authors report no conflict of interest.

Author ORCIDs.
Yuri V. Lvov https://orcid.org/0000-0003-2153-4047.

Appendix A. Averaging products of trees

Here, we perform in detail gluing the rest of the trees into a diagrammatic series for correlation functions. The gluing steps may be avoided altogether. We present them here for reference and to show how the $1/N$ symmetry rule appears.

A.1. *Three-point correlators of the third order*

In this subsection, we compute the three-point correlation function of the third order in the interaction vertex. This object is obtained by gluing together three trees and averaging over the ensemble of random force. The advantage of the diagrammatic technique is that the gluing of the trees representing perturbation expansions again can be omitted altogether.

Consequently, the diagrams for these three-point correlators of the third order in the vertices can be drawn from scratch. Construction of these diagrams can be achieved by exhausting all possible topologies consistent with the diagrammatic rules. We present the details of the calculations here to illustrate constructively the mechanism of appearance of the $1/N$ symmetry rule.

The terms

$$(2\pi)^{d+1}\delta^{d+1}_{123}\,{}^{3}\mathcal{F}^{(3)}_{123} = {}^{3}\mathcal{F}^{(3)}_{123}, \quad \mathcal{F}^{(3)}_{123} = {}^{3a}\mathcal{A}_{1,23} + {}^{3b}\mathcal{A}_{1,23} + {}^{3}\mathcal{B}_{12,3} + {}^{3}\mathcal{C}_{123}, \tag{A1a}$$

$${}^{3a}\mathcal{A}_{1,23} = \frac{\langle {}^{3a}a_1 a_2 a_3\rangle}{2}, \quad {}^{3b}\mathcal{A}_{1,23} = \frac{\langle {}^{3b}a_1 a_2 a_3\rangle}{2}\ {}^{3}\mathcal{B}_{12,3} = \langle a^2_1 a^1_2 a_3\rangle, \ \ {}^{3}\mathcal{C}_{123} = \frac{1}{3!}\,\langle a^1_1 a^1_2 a^1_3\rangle, \tag{A1b}$$

with one (${}^{3a}\mathcal{A}_{1,23}$ and ${}^{3b}\mathcal{A}_{1,23}$), two (${}^{3}\mathcal{B}_{12,3}$) and three (${}^{3}\mathcal{C}_{123}$) external $\mathcal{G}$ legs, respectively. Resulting diagrams are shown in figure 4. For consistency with previous notation, we denote by ${}^{3}\mathcal{A}$ third-order three-point correlators with one external Green's function, and by ${}^{3}\mathcal{B}$ third-order correlators with two external Green's functions. Consistently with previous definitions of $\mathcal{A}$ and $\mathcal{B}$ terms, we use notation ${}^{n}\mathcal{C}_{123,\ldots}$ for all diagrams of nth order in vertices V with three $\mathcal{G}$ legs $\mathcal{G}_1$, $\mathcal{G}_2$ and $\mathcal{G}_3$, and any number of wavy tails denoting $\mathcal{F}_j$.

We now consider each of these terms separately, one by one.

A.1.1. ${}^{3a}\mathcal{A}$ *terms*

The ${}^{3a}\mathcal{A}_{1,23}$ term after substitution of (2.8*c*) for ${}^{3a}a_1$ can be presented as

$${}^{3a}\mathcal{A}_{1,23} = \frac{\mathcal{G}_1\mathcal{G}^2_{\ldots}V^3_{\ldots}}{4}\,\langle (a_4a_5a_6a_7)_1(a_2a_3)_2\rangle. \tag{A2}$$

We now construct double correlators by pairing the fields (wavy lines). To get an irreducible contribution, we pair $[\overbrace{(7\text{-}(2}, 3)_2]$ (two options), then $[(\overbrace{3\text{-}(5}, 6)_2]$ (two options), and finally $\overbrace{4\text{-}6}$ (one option). The resulting diagram is shown in figure 4(*a*), and the corresponding analytical expression is given by (2.14*a*).

A.1.2. ${}^{3b}\mathcal{A}$ *terms*

The ${}^{3b}\mathcal{A}_{1,23}$ term after substitution of (2.8*d*) for ${}^{3b}a_1$ can be presented as

$${}^{3b}\mathcal{A}_{1,23} = \frac{\mathcal{G}_1\mathcal{G}^2_{\ldots}V^3_{\ldots}}{16}\,\langle (a_4a_5a_6a_7)_1(a_2a_3)_2\rangle. \tag{A3}$$

However, due to the different topology of the tree for ${}^{3b}a_q$, we should pair fields differently, e.g. as follows: $[(4, 5, 6, \overbrace{7)\text{-}2}]$ (four options), next $[(5, \overbrace{6)\text{-}3}]$ (two options), and finally $\overbrace{4\text{-}5}$ (one option). The resulting analytical expression is given by (2.14*b*), as shown diagrammatically in figure 4(*b*).

A.1.3. ${}^3\mathcal{B}$ *terms*

The ${}^3\mathcal{B}_{12,3}$ term after substitution of (2.8*a*) for ${}^1a_1$ and (2.8*b*) for ${}^2a_1$ can be presented as

$$ {}^3\mathcal{B}_{12,3} = \frac{\mathcal{G}_1 V_{\dots} \mathcal{G}_2 G_{\dots} V^2_{\dots}}{2^2} \langle (a_4 a_5)_1 ((a_6 a_7 a_8)_2) a_3 \rangle. \tag{A4} $$

To get an irreducible contribution, we should pair for example $[\overbrace{6\text{-}(4}, 5)]$ (two options), next $[\overbrace{3\text{-}(6}, 7)]$ (two options), and finally $\overbrace{7\text{-}5}$ (one option). As a result, we have four equivalent contributions to ${}^3\mathcal{B}_{12,3}$, as shown in (2.14*c*) and figure 4(*c*).

A.1.4. ${}^3\mathcal{C}$ *terms*

The ${}^3\mathcal{C}_{123}$ term can be presented as

$$ {}^3\mathcal{C}_{123} = \frac{(\mathcal{G}_1 \mathcal{G}_2 \mathcal{G}_3 V^3_{\dots})}{2^3 \times 3!} \langle (a_4 a_5)_1 (a_6 a_7)_2 (a_8 a_9)_3 \rangle. \tag{A5} $$

Pairing, for example, as $[\overbrace{4\text{-}(9}, 6, 7, 8)]$ (four options), $[(5, \overbrace{6\text{-}(7}, 8)]$ (two options) and $[\overbrace{5\text{-}8}]$ (one options), we have eight equal terms. The resulting diagram is figure 4(*d*), and the corresponding analytical expression is given by (2.14*d*).

A.2. *Four-point correlator leading terms*

Here we show how to glue four trees together to form the diagrammatic series for the four-point correlator in the second order in the interaction vertex. These steps are performed here in detail to demonstrate explicitly how the diagrammatic series for correlation functions appear, and why they have the factor corresponding to the $1/N$ symmetry rule. These steps are equivalent to those described in § 2.3.3 and may be omitted altogether by drawing the diagrams from scratch for the correlation functions as explained in § 2.4.

Consider first the expression for ${}^2\mathcal{B}_{12,34}$. Substituting expressions for ${}^1a_1$ and ${}^1a_2$ from (2.8*a*) and (2.8*b*), we obtain

$$ {}^2\mathcal{B}_{12,34} = \tfrac{1}{16} \mathcal{G}_1 \mathcal{G}_2 V_{156} V_{278} \langle (a_5 a_6)_1 (a_7 a_8)_2 (a_3 a_4)_3 \rangle. \tag{A6} $$

Here and below, subscripts 1 and 2 identify the tree from which the analytical structure appeared. Pairing fields in each $(\dots)_j$ group leads to uncoupled contribution. There are four equivalent ways to pair $[\overbrace{4\text{-}(5}, 6, 7, 8)]$, two ways to pair $[\overbrace{3\text{-}(7}, 8)]$, and one way to pair $\overbrace{6\text{-}8}$. The result, shown diagrammatically in figure 3(*c*), has corresponding analytical expression given in (2.16).

Next, substituting ${}^2a_q$ from (2.8*b*) in (2.15), we get

$$ {}^2\mathcal{A}_{1,234} = \frac{(\mathcal{G}V)}{2 \times 3!} \langle ((a_5 a_6 a_9)_1 (a_2 a_3 a_4)_2 \rangle. \tag{A7} $$

Required irreducible diagrams can be obtained from all possible (six) pairing of all three fields $(\dots)_1$ with all three fields $(\dots)_2$: $[(5, 6, \overbrace{9)_1\text{-}(2}, 3, 4)_2]$. The resulting analytical expression is given in (2.16) and is shown diagrammatically in figure 3(*b*).

A.3. *Fourth-order four-point correlator*

In this subsection, we glue four trees to obtain the expressions for the four-point correlators in the fourth order in the vertices.

Notice that we have met here the new type of diagrams ${}^{4}\mathcal{D}_{1234}$, where we preserved this notation for all diagrams of nth order in vertices V with four $\mathcal{G}$ legs, $\mathcal{G}_1$, $\mathcal{G}_2$, $\mathcal{G}_3$ and $\mathcal{G}_4$, and any number (including zero, as in this case) of wavy tails denoting $\mathcal{F}_j$.

A.3.1. ${}^{4a}\mathcal{A}_{1,234}$ *term*

After substitution of (2.8*e*) for ${}^{4a}a_1$, the ${}^{4a}\mathcal{A}_{1,234}$ term can be presented as

$$ {}^{4a}\mathcal{A}_{1,234} = \frac{G_1 G_{\dots}^3 V_{\dots}^4}{2 \times 3!} \langle a_2 a_3 a_4 (a_5 a_6 a_7 a_6 a_8 a_9)_1 \rangle. \tag{A8a} $$

Here we red-coloured terms originated from ${}^{4a}a_1$, and bracketed $(\dots)_1$ the corresponding field. A particular topological position of these terms and the rest of the fields is shown in figure 5(*a*), where (at this moment) we have to separate all wavy lines into two parts. Pairing, for example, as $[(4, 3, \overbrace{2)\text{-}5}]$ (three options), $[(4, \overbrace{3)\text{-}6}]$ (two options), $[\overbrace{4\text{-}(7}, 8)]$ (two options) and $[\overbrace{8\text{-}9}]$ (one option), we have 12 equal terms. The factor 12 fully compensates the denominator in (A8*a*), giving prefactor unity in the diagram for ${}^{4a}\mathcal{A}_{1,234}$. The results can be presented schematically as

$$ {}^{4a}\mathcal{A}_{1,234} = G_1 \mathcal{F}_2 \mathcal{F}_3 \mathcal{F}_4 G_{\dots}^3 V_{\dots}^3 \mathcal{F}_{\dots}. \tag{A8b} $$

An explicit analytical expression for ${}^{4a}\mathcal{A}_{1,234}$ can be reconstructed from figure 5(*a*) and is given by (A16*a*) below. The diagram for ${}^{4a}\mathcal{A}_{1,234}$ has only one element of symmetry, the identity, therefore the factor 1 in front of it is consistent with the $1/N$ rule.

A.3.2. ${}^{4b}\mathcal{A}_{1,234}$ *term*

After substitution of (2.8*f*) for ${}^{4b}a_1$, the ${}^{4b}\mathcal{A}_{1,234}$ term can be presented similarly to (A8*a*) as

$$ {}^{4b}\mathcal{A}_{1,234} = \frac{G_1 G_{\dots}^3 V_{\dots}^4}{4 \times 3!} \langle a_2 a_3 a_4 (a_5 a_6 a_7 a_6 a_8 a_9)_1 \rangle. \tag{A9} $$

However, as shown in figure 5(*b*), the topology of the corresponding tree is different. This different topology dictates a different way of pairing, for example $[(4, 3, \overbrace{2)\text{-}(5}, 6]$ (six options), $[\overbrace{6\text{-}(7}, 8))]$ (two options), $[\overbrace{8\text{-}(3}, 4)]$ (two options) and $[\overbrace{4\text{-}9}]$ (one option); we have 24 equal terms. Again, this fully compensates the denominator in (A9), giving prefactor unity in the diagram for ${}^{4b}\mathcal{A}_{1,234}$.

A.3.3. ${}^{4a}\mathcal{B}_{12,34}$ *term*

After substitution of (2.8*a*) for ${}^{1}a_1$ and (2.8*b*) for ${}^{2}a_2$, the ${}^{4a}\mathcal{B}_{12,34}$ term can be presented similarly to (A8*a*) and (A9) as

$$ {}^{4a}\mathcal{B}_{12,34} = \frac{G_1 G_2 G_{\cdots}^2 V_{\cdots}^4}{2^3} \langle a_3 a_4 (a_5 a_6 a_7 a_6 a_8)_2 (a_9 a_{10})_1 \rangle. \tag{A10} $$

Here, Green's functions and free fields originated from ${}^1a_1$ and ${}^2a_2$ are coloured in blue and green and are taken in parentheses $(\dots)_1$ and $(\dots)_2$. Their particular positions on the diagram for ${}^{4a}\mathcal{B}_{12,34}$, which dictate their pairing configuration, are shown in figure 5(*c*). The result that leads to this diagram is independent of the particular choice of strategy. For concreteness, we pair free fields ${}^0a_j$ in the following way: $[\overbrace{6\text{-}(3}, 4)]$ (two options), $[\overbrace{7\overbrace{4\text{-}(7}, 8)}]$ (two options), $[\overbrace{8\text{-}(9}, 10)]$ (two options) and finally $[\overbrace{5\text{-}10}]$ (one option). The resulting diagram is presented in figure 5(*c*), with the corresponding analytical expression given by (A16*c*) below. Note that again the numerical prefactor is equal to unity.

A.3.4. ${}^{4b}\mathcal{B}_{12,34}$ *term*

After substitution of (2.8*d*) for ${}^{3a}a_1$ and (2.8*a*) for ${}^1a_3$, the ${}^{4b}\mathcal{B}_{12,34}$ term can be presented similarly to (A8*a*) as

$$ {}^{4b}\mathcal{B}_{12,34} = \frac{G_1 G_3 G_{\cdots}^2 V_{\cdots}^4}{32} \langle (a_5 a_6 a_9 a_{10})_1 (a_7 a_8)_3 a_2 a_4 \rangle. \tag{A11} $$

Pairing as $[\overbrace{2\text{-}(5}, 6, 9, 10)]$ (four options), $[\overbrace{4\text{-}(10}, 9)]$ (two options), $[\overbrace{9\text{-}(8}, 7)]$ (two options) and finally $[\overbrace{4\text{-}10}]$ (one option), we have 16 equal terms, while the denominator in (A11) is 32. Therefore the result for ${}^{4b}\mathcal{B}_{12,34}$ has prefactor $1/2$, as shown graphically in figure 5(*d*), with the corresponding analytical expression given by (A16*d*) below.

Since the diagram has mirror symmetry with respect to the 1–3 diagonal, the factor $1/2$ in front of a diagram is consistent with our $1/N$ rule.

A.3.5. ${}^{4c}\mathcal{B}_{12,34}$ *term*

Using (2.8*b*) twice for ${}^2a_j$, the ${}^{4c}\mathcal{B}_{12,34}$ term is shown in figure 5(*e*) (if one breaks the wavy lines). Analytically, it can be presented as

$$ {}^{4c}\mathcal{B}_{12,34} = \frac{G_1 G_2 G_{\cdots}^2 V_{\cdots}^4}{2^4} \langle (a_5 a_6 a_{10})_1 (a_7 a_8 a_9)_2 a_3 a_4 \rangle. \tag{A12} $$

The additional prefactor $1/2$ is consistent with our $1/N$ rule since the diagram has two elements of symmetry: the identity, and rotation by π radians, which maps the diagram onto itself. An explicit analytical expression for ${}^{4c1}\mathcal{B}_{12,34}$ is given by (A16*e*) below and can be reconstructed from figure 5(*e*).

In (A16*e*), we denote the result as ${}^{4c1}\mathcal{B}_{12,34}$ because there is another contribution to ${}^{4c}\mathcal{B}_{12,34}$, which originates from a different way of pairing: $[\overbrace{4\text{-}(9}, 5, 6, 8)]$ (four options), then $[\overbrace{3\text{-}(5}, 6)]$ (two options), $[\overbrace{6\text{-}8}]$ (one option) and finally $[\overbrace{7\text{-}10}]$ (one option). Now we have again eight equal contributions to (A16*f*) below, which has denominator 16. This gives again prefactor $1/2$, reflecting mirror symmetry with respect to the horizontal line in the diagram for ${}^{4c2}\mathcal{B}_{12,34}$ shown in figure 5(*f*), with the corresponding analytical expression given by (A16*f*) below. In total,

$$ {}^{4c}\mathcal{B}_{12,34} = {}^{4c1}\mathcal{B}_{12,34} + {}^{4c2}\mathcal{B}_{12,34}. \tag{A13} $$

A.3.6. ${}^{4}\mathcal{C}_{123,4}$ *term*

After substitution of (2.8*b*) and (2.8*a*) for ${}^{2}a_1$, ${}^{1}a_3$ and ${}^{1}a_4$, the ${}^{4}\mathcal{C}_{123,4}$ term can be presented similarly to (A8*a*) as

$$ {}^{4}\mathcal{C}_{123,4} = \frac{G_1 G_3\, G_4 G_{\cdots} V_{\cdots}^4}{16} \langle (a_5 a_6 a_9)_1 a_2 (a_7 a_8)_3 (a_9 a_{11})_4 \rangle. \tag{A14} $$

Pairing, for example as $[\overbrace{2\text{-}(5}, 6)]$ (two options), $[\overbrace{6\text{-}(7}, 8, 10, 11)]$ (four options), $[\overbrace{8\text{-}10}, 11]$ (two options) and $[\overbrace{9\text{-}11}]$ (one option), we have 16 equal terms. Therefore the result for ${}^{4}\mathcal{C}_{1,234}$ has prefactor unity, with analytical expression shown in (A16*g*) below and depicted graphically in figure 5(*g*).

A.3.7. ${}^{4}\mathcal{D}_{1234}$ *term*

Substitution of (2.8*a*) for ${}^{1}a_j$ into (2.17) for ${}^{4}\mathcal{D}_{1234}$ gives

$$ {}^{4}\mathcal{D}_{1234} = \frac{G_1 G_2 G_3 G_4 V_{\cdots}^4}{2^4 \times 4!} \langle (a_5 a_6)_1 (a_7 a_8)_2 (a_9 a_{10})_3 (a_{11} a_{12})_4 \rangle. \tag{A15} $$

Pairing, for example as $[\overbrace{5\text{-}(7}, 8, 9, 10, 11, 12)]$ (six options) followed by the pairing $[\overbrace{8\text{-}(9}, 10, 11, 12)]$ (four options) and $[\overbrace{10\text{-}(11}, 12)]$ (two options), and pairing finally $[\overbrace{6\text{-}12}]$ (one option), we have 48 equal terms. Therefore the result for ${}^{4}\mathcal{D}_{1234}$, shown in figure 5(*h*), has prefactor $48/2^4\, 4! = 1/8$, consistent with the $1/N$ rule.

Corresponding analytical expressions are as follows:

$$ {}^{4a}\mathcal{A}_{1,234} = G_1 \mathcal{F}_2 \mathcal{F}_3 \mathcal{F}_4 \int \frac{\mathrm{d}\boldsymbol{q}_5}{(2\pi)^{d+1}} V_{18\bar{5}} V_{52\bar{6}} V_{63\bar{7}} V_{74\bar{8}} G_5 G_6 G_7 \mathcal{F}_8, \tag{A16a} $$

$$ {}^{4b}\mathcal{A}_{1,234} = G_1 \mathcal{F}_2 \mathcal{F}_3 \mathcal{F}_4 \int \frac{\mathrm{d}\boldsymbol{q}_5}{(2\pi)^{d+1}} V_{18\bar{5}} V_{52\bar{6}} V_{\bar{7}36} V_{\bar{8}74} G_5 \mathcal{F}_6 G_7^* G_8^*, \tag{A16b} $$

$$ {}^{4a}\mathcal{B}_{12,34} = G_1 G_2 \mathcal{F}_3 \mathcal{F}_4 \int \frac{\mathrm{d}\boldsymbol{q}_5}{(2\pi)^{d+1}} V_{18\bar{5}} V_{25\bar{6}} V_{63\bar{7}} V_{74\bar{8}} \mathcal{F}_5 G_6 G_7 \mathcal{F}_8, \tag{A16c} $$

$$ {}^{4b}\mathcal{B}_{12,34} = \frac{1}{2} G_1 \mathcal{F}_2 G_3 \mathcal{F}_4 \int \frac{\mathrm{d}\boldsymbol{q}_5}{(2\pi)^{d+1}} V_{18\bar{5}} V_{52\bar{6}} V_{36\bar{7}} V_{\bar{8}74} G_5 \mathcal{F}_6 \mathcal{F}_7 G_8^*, \tag{A16d} $$

$$ {}^{4c1}\mathcal{B}_{12,34} = \frac{1}{2} G_1 \mathcal{F}_2 G_3 \mathcal{F}_4 \int \frac{\mathrm{d}\boldsymbol{q}_5}{(2\pi)^{d+1}} V_{18\bar{5}} V_{52\bar{6}} V_{36\bar{7}} V_{74\bar{8}} G_5 \mathcal{F}_6 G_7 \mathcal{F}_8, \tag{A16e} $$

$$ {}^{4c2}\mathcal{B}_{12,34} = \frac{1}{2} G_1 \mathcal{F}_2 \mathcal{F}_3 G_4 \int \frac{\mathrm{d}\boldsymbol{q}_5}{(2\pi)^{d+1}} V_{18\bar{5}} V_{52\bar{6}} V_{\bar{7}36} V_{47\bar{8}} G_5 \mathcal{F}_6 G_7^* \mathcal{F}_8, \tag{A16f} $$

$$ {}^{4c}\mathcal{C}_{123,4} = G_1 \mathcal{F}_2 G_3 G_4 \int \frac{\mathrm{d}\boldsymbol{q}_5}{(2\pi)^{d+1}} V_{18\bar{5}} V_{52\bar{6}} V_{36\bar{7}} V_{47\bar{8}} G_5 \mathcal{F}_6 \mathcal{F}_7 \mathcal{F}_8, \tag{A16g} $$

$$ \mathcal{D}_{1234} = \frac{1}{8} G_1 G_2 G_3 G_4 \int \frac{\mathrm{d}\boldsymbol{q}_5}{(2\pi)^{d+1}} V_{18\bar{5}} V_{25\bar{6}} V_{36\bar{7}} V_{47\bar{8}} \mathcal{F}_5 \mathcal{F}_6 \mathcal{F}_7 \mathcal{F}_8. \tag{A16h} $$

Here, $\boldsymbol{q}_6 = \boldsymbol{q}_2 + \boldsymbol{q}_5$, $\boldsymbol{q}_7 = \boldsymbol{q}_3 + \boldsymbol{q}_6 = \boldsymbol{q}_2 + \boldsymbol{q}_3 + \boldsymbol{q}_5$ and $\boldsymbol{q}_8 = \boldsymbol{q}_5 - \boldsymbol{q}_1$.

Appendix B. Calculations of the simultaneous triple correlator in the third order in the vertex

To write down the corresponding analytical expression, we will choose the notation and direction of wave vectors according to $\boldsymbol{q}_5 = \boldsymbol{q}_1 + \boldsymbol{q}_4$ and $\boldsymbol{q}_6 = \boldsymbol{q}_4 - \boldsymbol{q}_2$. Diagrams ${}^{3a}A_{1,23}$ and ${}^{3b}A_{1,23}$ (both with prefactor $1/2$) produce two identical (under the permutation operator) twins.

Sums of these diagrams are shown in figures 7(*a*,*b*), now with prefactor unity. These diagrams have the Green's function G_5 oriented in different ways. The corresponding analytical expressions are given by

$$ {}^{3a}A^{I}_{1,23} = F_2F_3 \int \frac{\mathrm{d}\kappa_4\, T_{123}T_{356}T_{2346}}{(2\pi)^d}\, V_{14\bar5}V_{6\bar42}V_{53\bar6}F_4, \tag{B1a} $$

$$ {}^{3b}A^{I}_{1,23} = F_2F_3 \int \frac{\mathrm{d}\kappa_4\, T_{123}T_{246}T_{2345}}{(2\pi)^d}\, V_{14\bar5}V_{\bar426}V_{53\bar6}F_6. \tag{B1b} $$

Diagram ${}^{3}\mathcal{B}_{12,3}$, presented in figure 4(*c*) has three child diagrams shown in figures 7(*c*-i), 7(*c*-ii) and 7(*c*-iii), with the following analytical expressions:

$$ \left.\begin{aligned} {}^{3}B^{I}_{12,3} &= F_2 \int \frac{\mathrm{d}\kappa_4\, T_{123}T_{356}T_{2346}}{(2\pi)^d}\, V_{14\bar5}V_{6\bar42}V_{35\bar6}F_4F_6, \\ {}^{3}B^{II}_{12,3} &= F_3 \int \frac{\mathrm{d}\kappa_4\, T_{123}T_{246}T_{2345}}{(2\pi)^d}\, V_{14\bar5}V_{26\bar4}V_{35\bar6}F_5F_6, \\ {}^{3}B^{III}_{12,3} &= F_3 \int \frac{\mathrm{d}\kappa_4\, T_{123}T_{356}T_{1346}}{(2\pi)^d}\, V_{14\bar5}V_{2\bar46}V_{35\bar6}F_4F_5. \end{aligned}\right\} \tag{B2} $$

The procedure of 'multiplication' ensures that all the 'children' inherit the same combinations of the vertices and double correlators from their common parent, but differ in the frequency integrals.

Figure 4(*d*) with prefactor $1/6$ produces six identical twins and results in figure 7(*d*) now with prefactor unity. The analytical expression corresponding to these diagrams is given by

$$ {}^{3}C_{123} = \int \frac{\mathrm{d}\kappa_4\, T_{123}T_{246}T_{2345}}{(2\pi)^d}\, V_{145}V_{2\bar46}V_{35\bar6}F_4F_5F_6. \tag{B3} $$

Note that diagrams for ${}^{3b}A^{I}_{1,23}$, ${}^{3}B^{II}_{1,23}$ and ${}^{3}C_{123}$, shown in figures 7(*e*–*g*), have identical directions for all Green's functions and therefore have the same frequency integral, while diagrams for ${}^{3}B^{I}_{12,3}$ and ${}^{3}B^{III}_{12,3}$, shown in figures 7(*g*,*h*), have the same (but different from the previous set of diagrams) orientation of the Green's functions.

Appendix C. Square diagrams: details of calculations

Each of the eight diagrams for the quadruple correlator, depicted in figure 5 with analytical expressions (A16), involve four double correlators. Consequently, they produce $8 \times 2^4 = 128$ child diagrams, but only 22 of them, shown in figures 17 and 18, contribute to a simultaneous correlator.

The detailed are presented in § A.3.

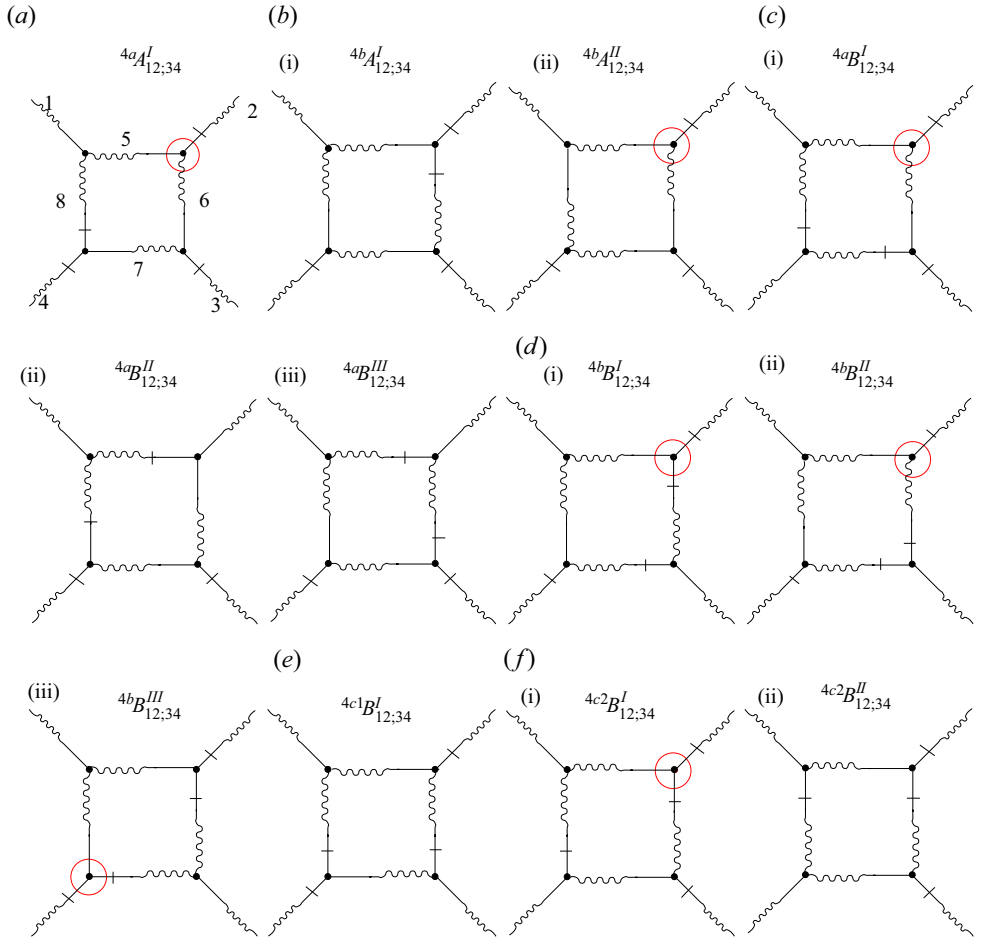

Figure 17. First group (A and B) of next-lowest (fourth) order 'child' diagrams for the simultaneous quadruple correlator ${}^{4}F_{1234}$.

The first diagram, ${}^{4a}A_{1,234}$, has only one surviving child, shown in figure 17(a):

$$ {}^{4a}A^{I}_{1,234} = F_2F_3F_4 \int \frac{\mathrm{d}\kappa_5\, T_{123}T_{356}T_{1346}}{(2\pi)^d}\, V_{18\bar{5}}V_{52\bar{6}}V_{63\bar{7}}V_{74\bar{8}}F_8. \tag{C1}$$

Diagram ${}^{4b}A_{1,234}$, depicted in figure 5(b), has two surviving children – see figures 17(b-i) and 17(b-ii). Corresponding analytical expressions are given by

$$ {}^{4b}A^{I}_{12;34} = F_2F_3F_4 \int \frac{\mathrm{d}\kappa_5\, T_{1234}T_{256}T_{2357}T_{23458}}{(2\pi)^d}\, V_{18\bar{5}}V_{52\bar{6}}V_{\bar{7}36}V_{\bar{8}74}F_6, \tag{C2a}$$

$$ {}^{4b}A^{II}_{12;34} = F_2F_3F_4 \int \frac{\mathrm{d}\kappa_5\, T_{1234}T_{367}T_{2357}T_{12378}}{(2\pi)^d}\, V_{18\bar{5}}V_{52\bar{6}}V_{\bar{7}36}V_{\bar{8}74}F_6. \tag{C2b}$$

These analytical expressions follow the same pattern: they have the same combination of vertices and double correlators. This appears to be the general rule for all children of the same parent diagram. These analytical expressions for the 'child' of the same parent

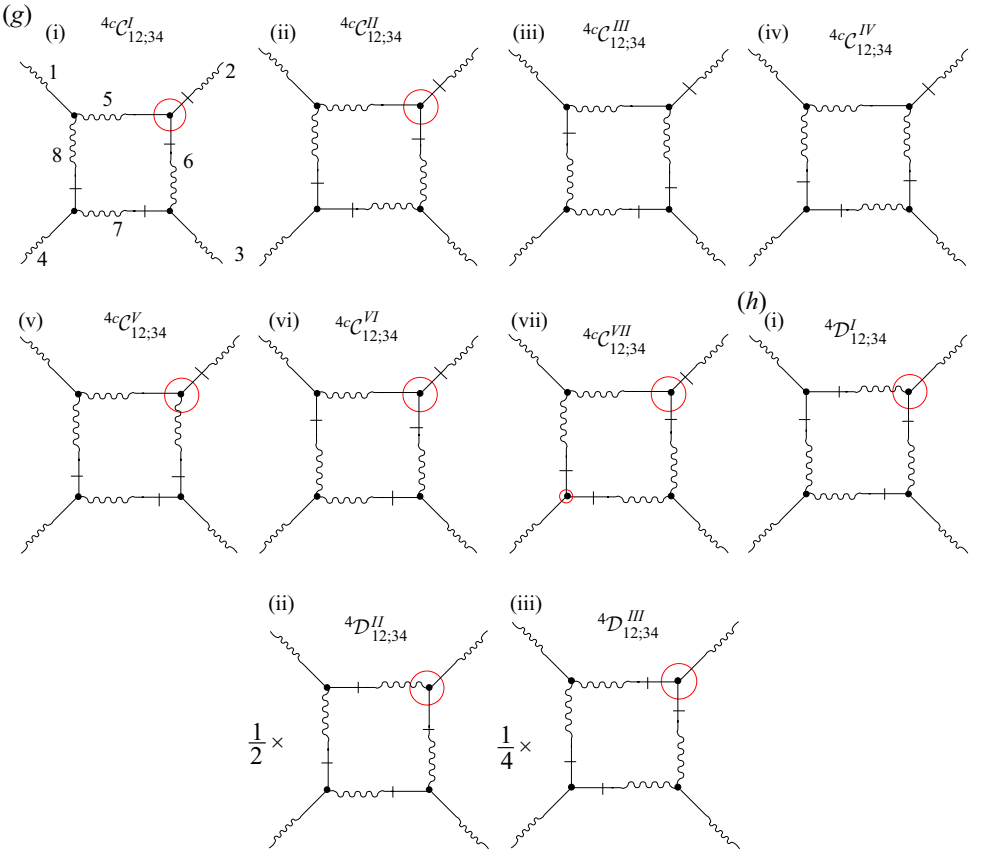

Figure 18. Second group ($\mathcal{C}$ and $\mathcal{D}$) of the next-lowest (fourth) order 'child' diagrams for the simultaneous quadruple correlator $^{4}F_{1234}$.

nevertheless do differ in frequency integrals. Diagrams $^{4a}B_{12,34}$ (figure 5(*c*) and (A16*c*)), have already three surviving children, shown in figure 17(*c*-i), 17(*c*-ii) and 17(*c*-iii).

Note that the total of 22 square diagrams for the four-point correlator of the fourth order presented in figures 17 and 18 depend only on very few (eight, to be exact) frequency integrals. This is due to the fact that the frequency integral depends only on the position and orientation of the Green's functions, and is independent of the vertices and whether the Green's function is 'true' or 'auxiliary'. Consequently, there are a lot of repeated frequency integrals, as seen in figures 17 and 18, and analytical expressions for these diagrams.

The analytical expressions corresponding to figures 17(*c*-i), 17(*c*-ii) and 17(*c*-iii) are given by

$$^{4a}B^{I}_{12,34} = F_3F_4\int \frac{\mathrm{d}\kappa_5\, T_{1234}T_{367}T_{23458}(T_{3468}+T_{2357})}{(2\pi)^d}\, V_{18\bar5}V_{25\bar6}V_{63\bar7}V_{74\bar8}F_5F_8, \quad \text{(C3}a\text{)}$$

$$^{4a}B^{II}_{12,34} = F_3F_4\int \frac{\mathrm{d}\kappa_5\, T_{1234}T_{478}T_{3468}T_{23458}}{(2\pi)^d}\, V_{18\bar5}V_{25\bar6}V_{63\bar7}V_{74\bar8}F_5F_8, \quad \text{(C3}b\text{)}$$

$$ {}^{4a}B^{III}_{12,34} = F_3F_4 \int \frac{\mathrm{d}\kappa_5\, T_{1234}T_{367}T_{23458}(T_{3468}+T_{2357})}{(2\pi)^d}\, V_{18\bar{5}}V_{25\bar{6}}V_{63\bar{7}}V_{74\bar{8}}F_5F_8. \quad \text{(C3}c\text{)} $$

Parent diagram ${}^{4b}\mathcal{B}_{12,34}$ (figure 5*d*) is symmetric with respect to rotation around the first and third legs. Therefore, in accordance with the $1/N$ rule, it has prefactor $1/2$. It has four children. The first two of them are rotationally symmetric and became identical (i.e. twins) under the permutation operator. They both contribute to diagram ${}^{4b}B^{I}_{12,34}$ (figure 17*d*-i), now without symmetry and with prefactor unity. The last two children are shown in figures 17(*d*-ii) and 17(*d*-iii), both symmetric and with prefactors $1/2$ as required by general diagrammatic rules. Their analytical expressions are

$$ {}^{4b}B^{I}_{12,34} = F_2F_4 \int \frac{\mathrm{d}\kappa_5\, T_{1234}T_{478}T_{3468}T_{23458}}{(2\pi)^d}\, V_{18\bar{5}}V_{52\bar{6}}V_{36\bar{7}}V_{\bar{8}74}F_6F_7, \quad \text{(C4}a\text{)} $$

$$ {}^{4b}B^{II}_{12,34} = \frac{F_2F_4}{2} \int \frac{\mathrm{d}\kappa_5\, T_{1234}T_{367}T_{2357}T_{12378}}{(2\pi)^d}\, V_{18\bar{5}}V_{52\bar{6}}V_{36\bar{7}}V_{\bar{8}74}F_6F_7, \quad \text{(C4}b\text{)} $$

$$ {}^{4b}B^{III}_{12,34} = \frac{F_2F_4}{2} \int \frac{\mathrm{d}\kappa_5\, T_{1234}T_{367}T_{23458}(T_{3468}+T_{2357})}{(2\pi)^d}\, V_{18\bar{5}}V_{52\bar{6}}V_{36\bar{7}}V_{\bar{8}74}F_6F_7. \quad \text{(C4}c\text{)} $$

Due to the nature of the 'multiplication' procedure, the 'children' repeat the parent's genome (combination of vertices and double correlators) but differ in frequency integrals.

The next diagram, ${}^{4c1}\mathcal{B}_{12;34}$ (figure 5(*e*) and (A16*e*)), with prefactor $1/2$, has two twins both contributing to figure 17(*e*), with corresponding analytical expression given by

$$ {}^{4c1}B^{I}_{12,34} = F_2F_4 \int \frac{\mathrm{d}\kappa_5\, T_{123}T_{356}T_{1346}}{(2\pi)^d}\, V_{18\bar{5}}V_{52\bar{6}}V_{36\bar{7}}V_{74\bar{8}}F_6F_8, \quad \text{(C5)} $$

where the factor $1/2$ was replaced by unity.

Diagram ${}^{4c2}\mathcal{B}_{12;34}$ (figure 5(*f*) and (A16*f*)) has two sets of two twins, shown in figures 17(*f*-i) and 17(*f*–ii). Following the $1/N$ rule, we now replace $\frac{1}{2} \Rightarrow 1$ in both diagrams. We therefore have

$$ {}^{4c2}B^{I}_{12,34} = F_2F_3 \int \frac{\mathrm{d}\kappa_5\, T_{1234}T_{478}T_{3468}T_{23458}}{(2\pi)^d}\, V_{18\bar{5}}V_{52\bar{6}}V_{\bar{7}36}V_{47\bar{8}}F_6F_8, \quad \text{(C6}a\text{)} $$

$$ {}^{4c2}B^{II}_{12,34} = F_2F_3 \int \frac{\mathrm{d}\kappa_5\, T_{1234}T_{256}T_{478}(T_{12467}+T_{23458})}{(2\pi)^d}\, V_{18\bar{5}}V_{52\bar{6}}V_{\bar{7}36}V_{47\bar{8}}F_6F_8. \quad \text{(C6}b\text{)} $$

The most 'prolific' diagram ${}^{4c}\mathcal{C}_{123,4}$ (figure 5(*g*) and (A16*g*)) has as many as seven children, shown in figures 18(*g*-i)–18(*g*-vii). Consistent with the logic of our multiplication procedure, they differ only in frequency integrals. The corresponding

analytical expressions are given by

$$ {}^{4c}C^{I}_{123,4} = F_2 \int \frac{\mathrm{d}\kappa_5\, T_{1234} T_{478} T_{3468} T_{23458}}{(2\pi)^d}\, V_{18\bar5} V_{52\bar6} V_{36\bar7} V_{47\bar8} F_6 F_7 F_8, \tag{C7a} $$

$$ {}^{4c}C^{II}_{123,4} = F_2 \int \frac{\mathrm{d}\kappa_5\, T_{1234} T_{256} T_{12378} (T_{2357} + T_{1268})}{(2\pi)^d}\, V_{18\bar5} V_{52\bar6} V_{36\bar7} V_{47\bar8} F_6 F_7 F_8, \tag{C7b} $$

$$ {}^{4c}C^{III}_{123,4} = F_2 \int \frac{\mathrm{d}\kappa_5\, T_{1234} T_{256} T_{2357} T_{23458}}{(2\pi)^d}\, V_{18\bar5} V_{52\bar6} V_{36\bar7} V_{47\bar8} F_6 F_7 F_8, \tag{C7c} $$

$$ {}^{4c}C^{IV}_{123,4} = F_2 \int \frac{\mathrm{d}\kappa_5\, T_{123} T_{356} T_{1346} T_{123} T_{356} T_{1346}}{(2\pi)^d}\, V_{18\bar5} V_{52\bar6} V_{36\bar7} V_{47\bar8} F_6 F_7 F_8, \tag{C7d} $$

$$ {}^{4c}C^{V}_{123,4} = F_2 \int \frac{\mathrm{d}\kappa_5\, T_{1234} T_{367} T_{2357} T_{12378}}{(2\pi)^d}\, V_{18\bar5} V_{52\bar6} V_{36\bar7} V_{47\bar8} F_6 F_7 F_8, \tag{C7e} $$

$$ {}^{4c}C^{VI}_{123,4} = F_2 \int \frac{d\,\kappa_5\, T_{1234} T_{256} T_{478} (T_{12467} + T_{23458})}{(2\pi)^d}\, V_{18\bar5} V_{52\bar6} V_{36\bar7} V_{47\bar8} F_6 F_7 F_8, \tag{C7f} $$

$$ {}^{4c}C^{VII}_{123,4} = F_2 \int \frac{\mathrm{d}\kappa_5\, T_{1234} T_{367} T_{23458} (T_{3468} + T_{2357})}{(2\pi)^d}\, V_{18\bar5} V_{52\bar6} V_{36\bar7} V_{47\bar8} F_6 F_7 F_8. \tag{C7g} $$

Finally, we give analytical expressions for $2^4 - 2 = 14$ children of diagram ${}^4\mathcal{D}_{1234}$ with prefactor $1/8$ (figure 5(*h*) and (A16*h*)), shown in figures 18(*h*-i)–18(*h*-iii). First, eight identical (under the permutation operator) twins together contribute to ${}^4D^{I}_{12;34}$ shown in figure 18(*h*-i). This diagram has no symmetries and therefore has prefactor unity. Figure 18(*h*-ii) includes four twins and has prefactor $1/2$ instead of the parent prefactor $1/8$, while the last diagram, figure 18(*h*-iii), includes only two twins and has prefactor $1/4$.

We now write down all analytical expressions for the D square diagrams:

$$ {}^{4c}D^{I}_{1234} = \int \frac{\mathrm{d}\kappa_5\, T_{1234} T_{256} T_{1268} T_{12467}}{(2\pi)^d}\, V_{18\bar5} V_{25\bar6} V_{36\bar7} V_{47\bar8} F_5 F_6 F_7 F_8, \tag{C8a} $$

$$ {}^{4c}D^{II}_{1234} = \int \frac{\mathrm{d}\kappa_5\, T_{1234} T_{158} T_{1268} T_{12378}}{2(2\pi)^d}\, V_{18\bar5} V_{25\bar6} V_{36\bar7} V_{47\bar8} F_5 F_6 F_7 F_8, \tag{C8b} $$

$$ {}^{4c}D^{III}_{1234} = \int \frac{\mathrm{d}\kappa_5\, T_{1234} T_{367} T_{23458} (T_{3468} + T_{2357})}{4(2\pi)^d}\, V_{18\bar5} V_{25\bar6} V_{36\bar7} V_{47\bar8} F_5 F_6 F_7 F_8. \tag{C8c} $$

Here, as before, $\boldsymbol{q}_6 = \boldsymbol{q}_2 + \boldsymbol{q}_5$, $\boldsymbol{q}_7 = \boldsymbol{q}_3 + \boldsymbol{q}_6 = \boldsymbol{q}_2 + \boldsymbol{q}_3 + \boldsymbol{q}_5$ and $\boldsymbol{q}_8 = \boldsymbol{q}_5 - \boldsymbol{q}_1$.

References

Boffeta, G., Celani, A. & Vergassola, M. 2000 Inverse energy cascade in two-dimensional turbulence: deviations from Gaussian behavior. *Phys. Rev.* E **61**, R29.

Boffetta, G. & Ecke, R.E. 2012 Two-dimensional turbulence. *Annu. Rev. Fluid Mech.* **44** (1), 427–451.

Frisch, U. 1995 *Turbulence: The Legacy of A.N. Kolmogorov*. Cambridge University Press.

Kolmogorov, A.N. 1941 Equations of turbulent motion in an incompressible fluid. *Dokl. Akad. Nauk SSSR* **30**, 299–303.

Kraichnan, R. & Montgomery, D. 1980 Two-dimensional turbulence. *Rep. Prog. Phys.* **43**, 547.

Landau, L.D. & Lifshitz, E.M. 1980 *Statistical Physics,* vol. 5. Butterworth Heinemann.

Landau, L.D. & Lifshitz, E.M. 2013 *Fluid Mechanics: Landau and Lifshitz: Course of Theoretical Physics,* vol. 6. Elsevier.

L'vov, V.S., Lvov, Y.V. & Pomyalov, A. 2000 Anisotropic spectra of acoustic turbulence. *Phys. Rev.* E **61** (3), 2586.

L'VOV, V.S., POMYALOV, A. & PROCACCIA, I. 2002 Quasi-Gaussian statistics of hydrodynamic turbulence in $4/3 + \varepsilon$ dimensions. *Phys. Rev. Lett.* **89** (6), 64501.

L'VOV, V.S. & PROCACCIA, I. 1995 Exact resummations in the theory of hydrodynamic turbulence: 0. Line-resummed diagrammatic perturbation approach. arXiv:chao-dyn/9502010.

MARTIN, P.C., SIGGIA, E.D. & ROSE, H.A. 1973 Statistical dynamics of classical systems. *Phys. Rev.* A **8**, 423–437.

POPE, S.B. 2000 *Turbulent Flows*. Cambridge University Press.

TABELING, P. 2002 Two-dimensional turbulence: a physicist approach. *Phys. Rep.* **362**, 1–62.

WYLD, H.D. 1961 Formulation of the theory of turbulence in an incompressible fluid. *Ann. Phys. (N.Y.)* **14**, 143–165.

ZAKHAROV, V.E. & L'VOV, V.S. 1975 Statistical description of nonlinear wave fields. *Radiophys. Quantum Electron.* **18** (10), 1084–1097.

ZAKHAROV, V.E., L'VOV, V.S. & MUSHER, S.L. 1972 Transient behavior of a system of parametrically excited spin waves. *Sov. Phys. Solid State* **14** (3), 1–6.

ZAKHAROV, V.E., L'VOV, V.S. & STAROBINETS, S.S. 1975 Spin-wave turbulence beyond the parametric excitation threshold. *Sov. Phys. Usp.* **17** (6), 896.